nature communications

Article

https://doi.org/10.1038/s41467-024-51578-1

Altered mitochondria-associated ER membrane (MAM) function shifts mitochondrial metabolism in amyotrophic lateral sclerosis (ALS)

Received: 27 October 2022

Accepted: 12 August 2024

Published online: 03 January 2025

Check for updates

Delfina Larrea[1,8] ✉, Kirstin A. Tamucci[1,2], Khushbu Kabra[2], Kevin R. Velasco[1], Taekyung D. Yun[1], Marta Pera[1], Jorge Montesinos[3,4], Rishi R. Agrawal[2], Carmen Paradas[5], John W. Smerdon[6], Emily R. Lowry[6], Anna Stepanova[7], Belem Yoval-Sanchez[7], Alexander Galkin[7], Hynek Wichterle[6] & Estela Area-Gomez[1,3,4,8] ✉

Mitochondrial function is modulated by its interaction with the endoplasmic reticulum (ER). Recent research indicates that these contacts are disrupted in familial models of amyotrophic lateral sclerosis (ALS). We report here that this impairment in the crosstalk between mitochondria and the ER impedes the use of glucose-derived pyruvate as mitochondrial fuel, causing a shift to fatty acids to sustain energy production. Over time, this deficiency alters mitochondrial electron flow and the active/dormant status of complex I in spinal cord tissues, but not in the brain. These findings suggest mitochondria-associated ER membranes (MAM domains) play a crucial role in regulating cellular glucose metabolism and that MAM dysfunction may underlie the bioenergetic deficits observed in ALS.

Amyotrophic lateral sclerosis (ALS) is a fatal neurological disorder characterized by the selective loss of motor neurons (MNs), resulting in muscle atrophy, paralysis, and respiratory failure[1]. Most ALS cases have an unknown etiology and are referred to as sporadic ALS (sALS). On the other hand, a growing number of mutations in more than 30 genes have been described and associated with familial ALS (fALS), with mutations in superoxide dismutase-1 (SOD1, gene *SOD1*) accounting for 12% of fALS cases[2]. The diverse functions of these genes implicate numerous cellular pathways and pathogenic processes in ALS progression. Yet, common to all forms of the disease, mitochondrial dysfunction, due primarily to a decrease in the activity of complex I (CI)[3], has been shown to precede the loss of MNs and play a central role in the development of the disease[4]. Another common feature shared by fALS and sALS is the deficit in metabolic flexibility. This refers to the essential capacity of cells to adapt to changes in energy demand and substrate availability, which depends on multiple mechanisms that modulate mitochondrial oxidative capacity to sustain cellular bioenergetics using carbon sources[5]. In particular, sALS and fALS cells present with defects in the uptake and oxidation of glucose[6], increased glycogen deposits[7], low insulin sensitivity, and high levels of fatty acids in blood[8], collectively indicating a substantial bioenergetic deficit in the context of ALS.

In most cell types, complex I (CI) is the main entry point of electrons into the respiratory chain for ATP production by the oxidation of

[1]Department of Neurology, Columbia University Irving Medical Center, New York, NY, USA. [2]Institute of Human Nutrition, Columbia University Irving Medical Center, New York, NY, USA. [3]Department of Biomedicine, Centro de Investigaciones Biológicas Margarita Salas (CSIC), Madrid, Spain. [4]Centro de Investigación Biomédica en Red Sobre Enfermedades Neurodegenerativas (CIBERNED), Madrid, Spain. [5]Department of Neurology, Instituto de Biomedicina de Sevilla, Hospital Universitario Virgen del Rocío, Seville, Spain. [6]Department of Pathology and Cell Biology, Columbia University Irving Medical Center, New York, NY, USA. [7]Brain and Mind Research Institute, Weill Cornell Medical College, New York, NY, USA. [8]These authors contributed equally: Delfina Larrea, Estela Area-Gomez. ✉e-mail: delfinalarrea21@gmail.com; estela.area@cib.csic.es

NADH and the transfer of electrons to Coenzyme Q (CoQ). In addition, CI acts as an essential hub for the integration and modulation of metabolic signaling routes in response to changes in nutritional status[9] and cellular redox state[10]. In addition to CI activity, the oxidation of succinate by CII (or succinate dehydrogenase, SDH) also contributes to oxidative phosphorylation (OxPhos) by the production of $FADH_2$ and the subsequent reduction of CoQ into $CoQH_2$. However, succinate oxidation by CII does *not* result in the translocation of protons into the intermembrane space and, therefore, yields fewer ATP molecules compared to NADH oxidation by CI[11]. Consequently, cells with high energy demands, like neurons, rely mostly on NADH oxidation by CI for ATP production, and display elevated NADH:$FADH_2$ ratios compared to other cell types[12].

The availability of these reducing equivalents (NADH and $FADH_2$) depends on the nature of the oxidizable substrate or carbon source. Pyruvate derived from the breakdown of glucose is the most common and efficient mitochondrial fuel source for sustaining high rates of NADH production[13]; however, when the availability of glucose-derived pyruvate is limited, other substrates such as fatty acids (FAs) and amino acids (AAs) are used as carbon sources for ATP production[14,15]. As opposed to pyruvate, the oxidation of FAs and, to a lesser extent, AAs results in increases in succinate, which boosts the flow of electrons from CII to CoQ via $FADH_2$[12]. Moreover, high $FADH_2$ levels induce the activation of enzymes that contain covalently linked FAD^+ cofactors (e.g., electron transferrin flavoproteins or ETFDH), which also contribute to the transfer of electrons to CoQ to form $CoQH_2$.

When sustained over time, high $CoQH_2$ levels exceed the capacity of this reduced CoQ pool to transfer electrons to CIII, causing electrons to subsequently flow backward to CI in a process called reverse electron transfer (RET)[16]. Under RET conditions, NAD^+ is reduced at CI, boosting NADH pools, albeit at the expense of higher rates of superoxide ($O_2^{\cdot-}$) production and the concomitant activation of superoxide dismutases[17,18]. To mitigate ROS increases under RET, CI undergoes a conformational transition from an active (A) to a dormant (D) state, attenuating oxidative damage[19]. Furthermore, under conditions of sustained RET, NADH elevations can inhibit the activity of many enzymes involved in glycolysis and FA metabolism[20,21].

The cellular mechanisms by which mitochondria balance the oxidation of different nutrients are not completely understood, but recent work has revealed that the contacts between mitochondria and a specific domain of the endoplasmic reticulum (ER), called mitochondria-associated ER membranes (MAM), contribute to pyruvate availability and oxidation in mitochondria[22,23]. MAM is a dynamic lipid-raft subdomain of the ER where specific enzymes co-localize for the concomitant regulation of numerous cellular pathways, including cellular nutrient and lipid metabolism[24]. Importantly, impairments in the formation of MAM have been associated with the pathogenesis of several neurodegenerative diseases[25–27], including ALS[28–30].

In this work, we show that MAM defects are present in sALS and fALS models with mutations in *SOD1* that, in turn, disrupt pyruvate metabolism and shift ALS cells towards the use of alternative mitochondrial fuels, such as FAs. Over time, this metabolic shift results in the induction of RET, the inactivation of CI, and ultimately a bioenergetic crisis. Overall, our data support the role of MAM in the maintenance and regulation of glucose metabolism and suggest that MAM dysfunction is the origin of the characteristic mitochondrial alterations observed in ALS.

Results

Mitochondrial respiratory defects in *SOD1*-mutant ALS models are progressive and substrate-dependent

Mitochondrial bioenergetic deficiency is a common phenotype in all forms of ALS, but its cause is still unclear[31]. Multiple reports have implicated SOD1 as a mediator of the mitochondrial disturbances in the disease, both when it is mutated in fALS and when it is misfolded in sALS[32,33]. To understand the origin of these metabolic alterations, we confirmed that the transgenic mouse model of ALS used here [overexpressing human *SOD1* carrying the *G93A* mutation ($SOD1^{G93A}$)] indeed displayed mitochondrial deficiencies in the brain and spinal cord (SPC) compared to age-matched non-transgenic (NTg) controls. We performed double histochemical staining to visualize the activities of complex IV (CIV, cytochrome *c* oxidase) and complex II (CII, succinate dehydrogenase), a method that enables the detection of cells with mitochondrial dysfunction in situ[34,35]. In agreement with previous data[36], we found that brain and SPC samples from $SOD1^{G93A}$ animals displayed defects in the respiratory chain at a pre-symptomatic stage (P60) (Fig. 1).

We next measured oxygen consumption rates (OCR) in mitochondria isolated from brain and SPC tissues from age-matched and

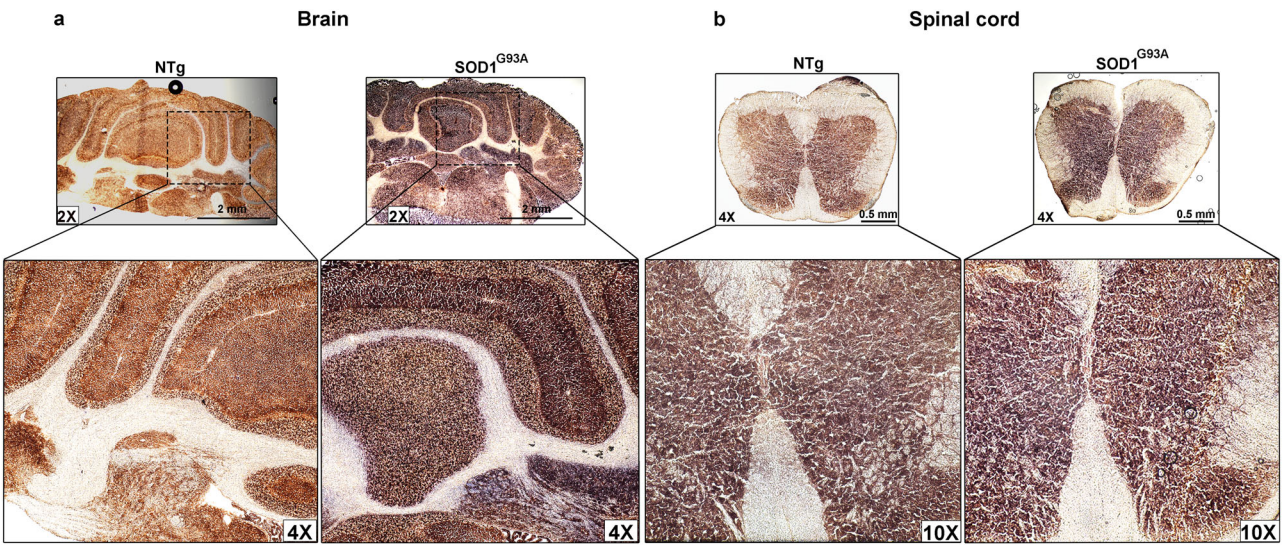

Fig. 1 | Defects in mitochondrial respiratory complexes in tissues from $SOD1^{G93A}$ mice. a Cytochrome *c* oxidase (COX) and succinate dehydrogenase (SDH) activities are shown by double staining in 20-µm-thick coronal sections of the cerebellum and **b** in cross sections of SPC tissues from $SOD1^{G93A}$ and NTg (control) mice at pre-symptomatic stage P60. Note that, in control sections, the purple stain representing SDH activity is masked by the brown stain representing COX activity, whereas the purple stain is prominently visible in mutant tissues. This suggests that COX activity is reduced in mutant samples, enabling visualization of the SDH stain. The images shown are representative of 3 independent animals per group.

sex-balanced SOD1^{G93A} mice and NTg controls. To avoid the confounding effects of significant neuronal death and of astro- or microgliosis on oxygen consumption[37], we performed our analyses on mitochondria isolated from tissues at different pre-symptomatic ages (P15, P30, P60) and compared the results to analyses conducted at disease onset (P90) and late (P120) stages (Fig. 2a–d, Supplementary Fig. 1a and Supplementary table 1). Respiration was measured using pyruvate (in the presence of malate to inhibit CII activity), the oxidation of which activates NADH-CI-driven oxygen consumption (NADH-OCR) (Fig. 2a, c). Respiration was also measured using succinate as the substrate (in the presence of rotenone to inhibit CI activity), as succinate oxidation produces higher levels of $FADH_2$ compared to the oxidation of pyruvate[38], and thus activates $FADH_2$-CII-driven oxygen consumption ($FADH_2$-OCR)[39](Fig. 2b, d).

At the earliest stage examined (P15), mitochondria isolated from SOD1^{G93A} brain showed a slight reduction in NADH-OCR at baseline (respiratory state 2), but significantly increased OCR after stimulation with ADP (state 3), and a sustained elevation in states 4 and 3U (Fig. 2a). This elevation was not observed at P30 or P60, nor at symptomatic stages (P90 and P120) (Fig. 2a). As opposed to brain mitochondria, those from SOD1^{G93A} SPC showed a progressive decline in NADH-OCR even at pre-symptomatic stages (Fig. 2b). We noted that the decline in NADH-OCR was in the range of 30–50%, as observed by others[40].

We then measured $FADH_2$-OCR and found significant changes in both the brain and SPC, especially at later stages of the disease. In SOD1^{G93A} brain, there was a progressive reduction in $FADH_2$-OCR (> 30%) that was maintained at disease onset (P90), but increased significantly over NTg levels during end-stages of the disease (P120) (Fig. 2c). In SOD1^{G93A} SPC, the progressive decline in $FADH_2$-OCR began earlier (at P30) and was more pronounced (> 50%) than the decline in NADH-OCR at P60 (Fig. 2d). Also, we observed that $FADH_2$-OCR increased up to NTg levels during disease end-stages (Fig. 2d), perhaps due to a significant proliferation of glial cells in mouse ALS tissues. Taken together, SOD1^{G93A} brain mitochondria presented with slight reductions in NADH- and $FADH_2$-OCR at pre-symptomatic and early-onset stages, but these reductions did not reach the threshold considered to be pathogenic[41]. On the other hand, SOD1^{G93A} SPC mitochondria presented earlier with more significant reductions in $FADH_2$-OCR compared to NADH-OCR in the brain and NTg controls. Altogether, we find that CI-driven oxygen consumption (NADH-OCR) declines after P60 in SOD1^{G93A} brain (Fig. 2a) and even earlier, after P30, in SOD1^{G93A} SPC (Fig. 2b). Meanwhile, CII-driven respiration ($FADH_2$-OCR) increases after P60 in both tissues (Fig. 2c, d).

To determine whether the alterations in $FADH_2$-OCR in SOD1^{G93A} tissues were due to deficits in the catalytic capacity of CII, we measured CII activity as succinate dehydrogenase at a pre-symptomatic (P60) stage. Despite the reductions in $FADH_2$-OCR observed in SOD1^{G93A} tissues at P60 (Fig. 2a, d), CII activity was not significantly altered in SOD1^{G93A} brain and ~25% reduced in SOD1^{G93A} SPC compared to NTg controls (Fig. 2e). Moreover, we did not find any changes in the levels of mitochondrial respiratory chain components (Supplementary Fig. 1b), mitochondrial biogenesis markers (Supplementary Fig. 1c), or mtDNA content (Supplementary Fig. 1d). This result implies that CII is enzymatically intact. Nonetheless, the decline in $FADH_2$-CII-driven OCR is more pronounced than the decline in NADH-CI-OCR, even before disease onset. This finding was unexpected since the central nervous system is considered to rely almost exclusively on NADH[14], meaning that OCR defects are expected to be driven by alterations in CI, rather than CII.

To better understand these mitochondrial phenotypes, we calculated the respiratory control ratio (RCR) (i.e., ratio of state 3:state 4) under both substrates (pyruvate and succinate) as a measure of the coupling efficiency between mitochondrial respiration and ATP production[42]. RCR values showed only slight differences between NTg and SOD1^{G93A} mitochondria when pyruvate was used as the substrate (NADH-OCR). However, succinate oxidation ($FADH_2$-OCR) resulted in significantly higher RCR values in mitochondria from SOD1^{G93A} brain and SPC relative to NTg controls (Fig. 2f). A higher RCR indicates a greater capacity for ATP production[43], suggesting here that, despite showing reductions in $FADH_2$-OCR, mitochondria from SOD1^{G93A} mice use succinate in a slightly more efficient manner than pyruvate.

Since motor neurons (MNs) are the most impaired cell type in ALS, we measured the mitochondrial respiratory profile (in the presence of pyruvate and glucose) of non-permeabilized, cultured human embryonic stem cell (ESC)-derived MNs carrying a mutation in *SOD1* (*SOD1*$^{+/A4V}$; denoted as hMNs^{A4V}) and WT controls, on different days in vitro (DIV) (Fig. 2g). Mutant hMNs^{A4V} displayed elevated OCR values at DIV2 that declined over time to ~ 50% of WT hMNs at DIV14 (Fig. 2g and Supplementary Fig. 1e), in agreement with what has been shown by others[44]. In addition, hMNs^{A4V} showed a lower spare respiratory capacity (SRC; uncoupled respiration minus basal respiration) compared to WT controls, indicating a significant deficit in mitochondrial metabolic flexibility (Supplementary Fig. 1f), whereas no significant change was found in proton leak (Supplementary Fig. 1i). The defects in hMNs^{A4V} mitochondrial respiration coincided with an increase in mitochondrial biogenesis (Supplementary Fig. 1g) and mitochondrial mass (Supplementary Fig. 1h).

To test the capability of pyruvate and succinate to feed electrons into the respiratory chain, we repeated the respirometry assays in permeabilized hMNs. As before, hMNs^{A4V} at DIV7 and DIV14 fed with pyruvate (NADH-OCR) showed no alterations in OCR at state 2 (no ADP) but showed reductions after the addition of ADP (state 3) (Fig. 2h, right panel) when respiration is driven by ATP hydrolysis[42]. This data indicates that hMNs^{A4V} are less responsive to pyruvate-driven ADP stimulation but maintain normal OCR at state 2. These results are consistent with a scenario in which electrons derived from pyruvate (or other NADH substrates) are not efficiently used by the respiratory chain for ATP production, and are leaked from mitochondria to avoid ROS production[42]. On the other hand, similar to SOD1^{G93A} mitochondria, the respiratory defects in hMNs^{A4V} were worsened when succinate was used as the substrate, appearing even at baseline before the addition of ADP (Fig. 2h, left panel).

The difference between the oxygen consumption levels when using pyruvate versus succinate points to an alteration in the flow of electrons in ALS mitochondria. This suggests that the electron flux via CII is greater in ALS than in healthy tissues. This could, in turn, induce a shift from NADH-linked substrates, like pyruvate, towards $FADH_2$-linked fuels, such as fatty acids (FAs), to produce ATP, as has been shown to occur in muscle tissues[45].

A shift to fatty acid oxidation induces reverse electron transfer and the transition of CI to the dormant state in SOD1^{G93A} mice

Defects in the metabolism of glucose (i.e., the oxidation of pyruvate) and increases in the oxidation of fat sources have been observed in ALS patient samples, cells, and mouse models[6,45]. In support of these findings, we found that hexokinase (HK) activity, the first rate-limiting enzyme of glycolysis, was progressively reduced in brain and SPC tissues from SOD1^{G93A} mice compared to controls (Fig. 3a). Similarly, we found significant reductions in pyruvate dehydrogenase complex (PDHC) activity, which converts pyruvate into acetyl-CoA to feed the TCA cycle, in mitochondria from both SOD1^{G93A} brain and SPC at pre-symptomatic stages and at disease onset (Fig. 3b). Likewise, hMNs^{A4V} presented with gradual reductions in HK and PDHC activities compared to WT controls (Fig. 3c, d), in agreement with the known decline in glucose metabolism in ALS[6]. In all cases, mRNA expression for these genes was essentially unchanged compared to controls (Supplementary Fig. 2a).

Neuronal pyruvate pools are primarily derived from astrocytic lactate that is converted to pyruvate by lactate dehydrogenase (LDH)[13]. We therefore measured LDH activity in our hMN cultures and found

https://doi.org/10.1038/s41467-024-51578-1

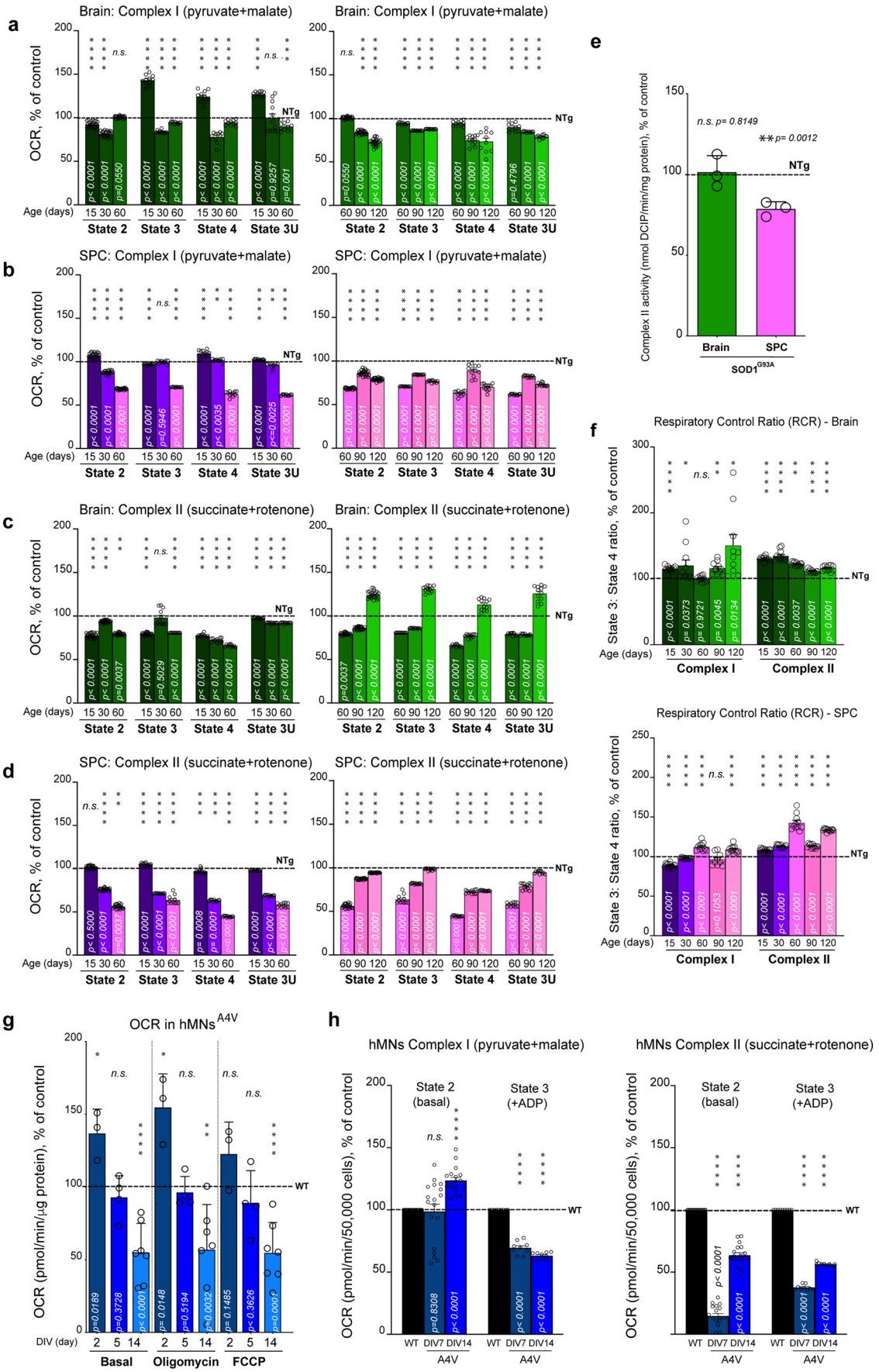

Fig. 2 | Progressive alterations in mitochondrial respiration in SOD1^{G93A} mice. Oxygen consumption rate (OCR, in pmole O_2/min/mg protein) in mitochondria isolated from brain (**a**, **c**) and spinal cord (SPC) (**b**, **d**) from SOD1^{G93A} mice at the indicated ages (in days) compared to age-matched NTg controls (set at 100%; dotted lines) at states 2/3/4/3U. The columns represent the mean ± SE. $n = 4$ biological replicates consisting of a pool of tissues from 4 animals (2 male and 2 female). Dots indicate the OCR average at the specific time point using Seahorse (see methods). **e** Complex II enzymatic activity in isolated mitochondria from SOD1^{G93A} tissues at P60 relative to the NTg control average (set at 100%; dotted line). Data represent the mean ± SD; $n = 3$ biologically independent samples (2 male and 1 female). **f** RCR (ratio of state 3: state 4) calculated from the respiratory values in Fig. 2 (**a**–**d**) in SOD1^{G93A} brain (top panel) and SPC (bottom panel) mice relative to the NTg control average (set at 100%; dotted lines). The columns represent the mean of the RCR ± SE; $n = 4$. Dots indicate the relative RCR values of SOD1^{G93A} relative to NTg of each group at the specific time point (set at 100%; dotted lines). **g** OCR in hMNs^{A4V} relative to WT controls (set at 100%; dotted lines) in the presence of pyruvate as a mitochondrial substrate. Data represent the mean ± SD; $n = 3$ (DIV2), $n = 5$ (DIV5) and $n = 7$ (DIV14). **h**, **i** NADH- and $FADH_2$-OCR in permeabilized hMNs^{A4V} relative to WT controls (set at 100%; dotted lines). Data represent the mean ± SE. $n = 4$. Statistical test: Student's two-tailed *t*-test for normal data or the Mann-Whitney *U* test for non-normal data at an $\alpha = 0.05$ significance level. Statistical significance is shown as: n.s. $p>0.05$; * $p<0.05$; ** $p<0.01$; *** $p<0.001$; **** $p<0.0001$.

significant decreases in the hMN^{A4V} mutants (Fig. 3e), despite showing higher expression levels of *LDHA* mRNA (Supplementary Fig. 2b). Taken together, these results support a decline in the production and use of pyruvate in neural tissues of SOD1^{G93A} mice and hMNs^{A4V} compared to controls and, thus, a decrease in the utilization of pyruvate as a substrate for mitochondrial respiration. In light of these data, we tested the use of FAs as an alternative mitochondrial fuel source by measuring the activity of carnitine palmitoyl-transferase 1 (CPT1). This enzyme conjugates carnitine to long-chain FAs (C_{12} to C_{20}) for their translocation into mitochondria and subsequent oxidation. We found that CPT1 activity showed a trend of being higher in mitochondria isolated from SOD1^{G93A} brains at symptomatic stages, contrary to SPC, which showed no significant changes compared to controls (Fig. 3g). On the other hand, hMNs^{A4V} showed an early increase in CPT1 activity at DIV2 followed by a progressive reduction at DIV14 (Fig. 3f), even though *Cpt1* expression was unchanged (Supplementary Fig. 2c).

To further examine this phenotype, we quantified the levels of FAs bound to carnitine (i.e., acylcarnitines, ACs) by lipidomics analysis of total homogenates and crude mitochondria fractions from SOD1^{G93A} tissues and NTg controls (Fig. 3h). In SOD1^{G93A} mouse brain, we found significant elevations in the longer FA chains (AC_{14} to AC_{18}), indicative of increased usage of FAs as mitochondrial substrates[46], while the concentrations of shorter AC species were reduced (right panel). On the other hand, in SPC from SOD1^{G93A} mice and in hMNs^{A4V}, we found significantly increased levels of short ACs (AC_2 to AC_8) and reductions in longer AC species (Fig. 3h). Notably, increases in short-chain ACs have been shown to arise from incomplete β-oxidation of FAs in mitochondria[47], which suggests that FA oxidation in mutant SPC was disrupted compared to brain.

As mentioned above, under conditions of increased FA oxidation, the levels of succinate and $FADH_2$ increase and trigger reverse electron transfer (RET)[48,49]. Cells under RET display reduced NAD^+:NADH ratios and increased membrane potential[50]. Consistent with the activation of RET in our mutant mice, mitochondria from SOD1^{G93A} brain and SPC at P60, as well as those from hMNs^{A4V}, had significantly lower NAD^+:NADH ratios compared to controls (Fig. 4a).

The reduction of NAD^+ to form NADH during RET is also associated with high rates of ROS production[17,51] that, if persistent, result in reductions in CI activity[48,49]. In line with this idea, SOD1^{G93A} mitochondria from SPC, but not the brain, showed a significant increase in the production of H_2O_2 when pyruvate, but not succinate, was used as substrate (Fig. 4b). These data suggest that, even under RET conditions, mitochondria from SOD1^{G93A} brain tissues maintain a pool of CI that is working in forward mode (i.e., oxidizing NADH). Conversely, our results indicate that NADH-linked substrates trigger the production of ROS in SOD1^{G93A} SPC, perhaps implying that a higher proportion of SPC CI could be working in reverse mode (i.e., reducing NAD^+)[19].

To attenuate the oxidative damage associated with RET, CI becomes transiently deactivated via conformational changes as a counterbalancing mechanism[10]. Therefore, to corroborate our data, we measured the kinetics of the transition from the catalytically deactivated, or dormant, "D-form" of CI to the fully active "A-form"[10,19] in mitochondria from brain and SPC of SOD1^{G93A} mice (Fig. 4c). Brain mitochondria from SOD1^{G93A} mice at P15 and P90 showed significant increases in the rate of CI activation, whereas mutant SPC mitochondria showed the opposite phenotype, but only upon disease onset (P90) (Fig. 4c and Supplementary Fig. 3). As before, these data further support the finding that, while the SOD1^{G93A} mouse brain can boost the pool of active CI, this complex is found predominantly in the D-form in SPC mitochondria.

Taken altogether, our data indicate that, in the context of SOD1 mutations, defects in the use of NADH substrates induce a shift toward the oxidation of FAs to generate ATP. This metabolic change results in elevations in $FADH_2$-CII-driven respiration and the subsequent activation of RET. This activation of RET induces increases in ROS production and the deactivation of CI in mutant SPC, but not in the brain. Our data thus support previously observed reductions in CI activity in an ALS model[52] but imply that, rather than being defective, CI in SPC tissues from ALS models is inactivated.

Alterations in glucose metabolism in *SOD1*-mutant models are induced by MAM disruption

The regulation of glucose metabolism and the use of pyruvate as a mitochondrial substrate has been shown to be modulated by the formation of MAM domains[23]. Indeed, glycolytic enzymes such as hexokinase 2 (HK2) have been shown to localize to MAM[53,54], and a growing number of reports have suggested that MAM domains and ER-mitochondria crosstalk are disrupted in the context of ALS[25,30]. Therefore, we asked whether the impairments in pyruvate metabolism found in the ALS models studied here were the consequence of defects in the formation and/or activation of MAM domains.

We measured ER-mitochondria crosstalk by quantifying the synthesis and transport of phospholipids between the two organelles, a well-established measure of MAM functionality[55] (Fig. 5b, d). In this dynamic assay, we found no significant changes in MAM activity in SOD1^{G93A} mouse brain compared to NTg controls at all ages analyzed (Supplementary Fig. 4a). In contrast, SOD1^{G93A} mouse SPC showed a progressive decline in MAM activity compared to NTg controls, reaching statistical significance at disease onset (P90) (Fig. 5b). Using the same approach, we also found significant reductions in MAM activity (at 6 h) in hMNs^{A4V} at DIV14 compared to WT controls (Fig. 5c). Similarly, these significant reductions in MAM activity were also found in hMNs derived from sALS cells at DIV14 (Fig. 5d), in cultured mouse embryonic stem cell (ESC)-derived MNs carrying the G93A mutation in *SOD1*^{G93A} (Supplementary Fig. 4b), in fibroblasts from sALS patients (Supplementary Fig. 4c, d), and in fibroblasts from fALS patients with other mutations in *SOD1* and *FUS* (Supplementary Fig. 4c, d).

In support of these results, SPC from SOD1^{G93A} mice and hMNs^{A4V} (Supplementary Fig. 2d, e) showed reductions in the expression of Mitofusin-2 (Mfn2), a MAM-localized protein that acts as an ER-mitochondria tether[56].

As a lipid raft, MAM is a transient domain induced by the clustering of cholesterol, sphingomyelin (SM), and saturated phospholipids[57] that recruits and modulates specific subsets of

https://doi.org/10.1038/s41467-024-51578-1

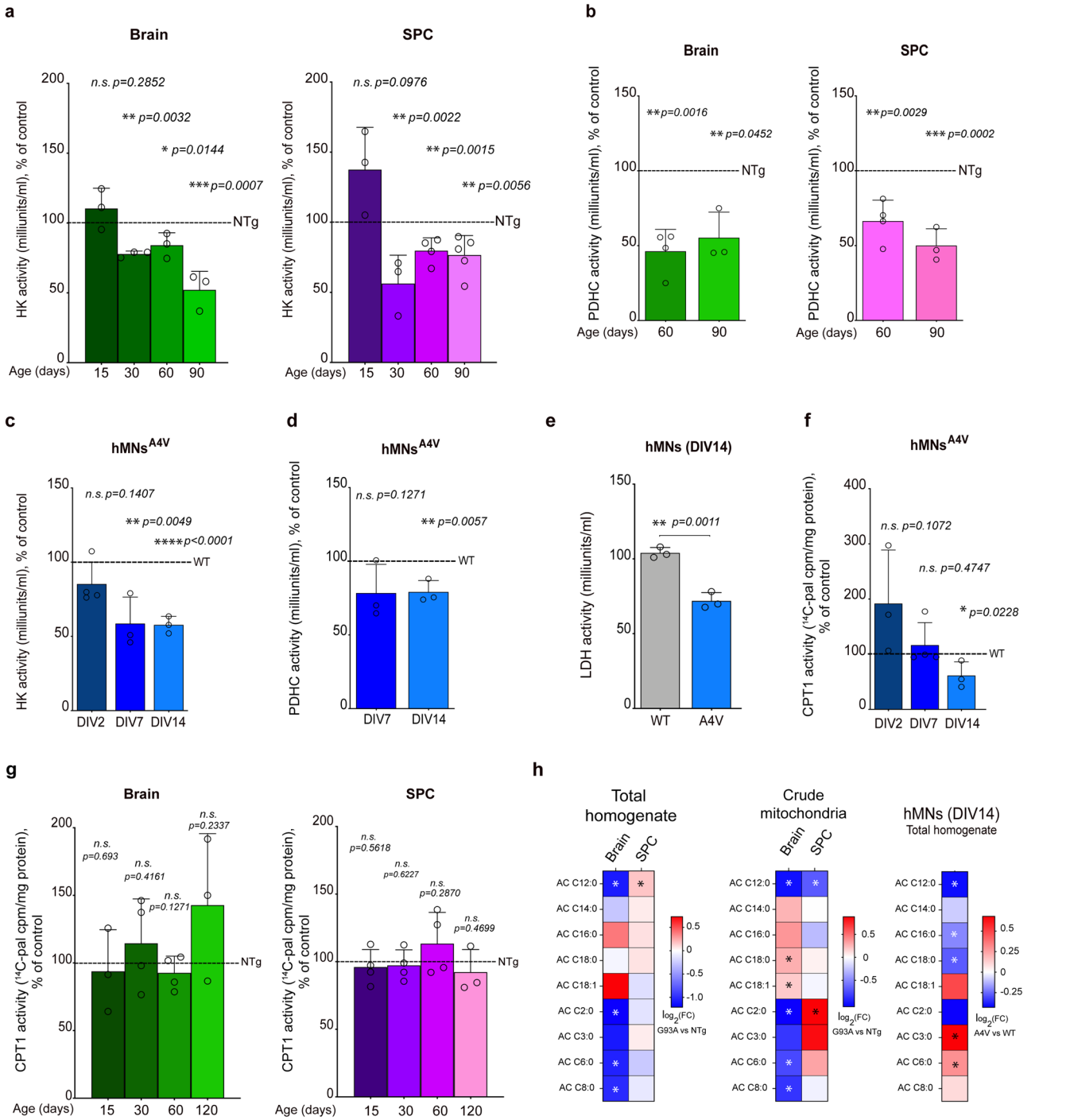

Fig. 3 | Defects in glycolysis and pyruvate metabolism in ALS models shift mitochondria towards fatty acid oxidation. a Hexokinase (HK) activity in total homogenates of brain and SPC from SOD1^{G93A} mice at the indicated ages relative to NTg control average (set at 100%; dotted line). The columns represent the mean ± SD. Brain: $n = 3$ (P15), $n = 3$ (P30), $n = 3$ (P60), $n = 3$ (P90); SPC: $n = 3$ (P15), $n = 3$ (P30), $n = 4$ (P60), $n = 5$ (P90) biologically independent samples. **b** Pyruvate dehydrogenase complex (PDHC) activity in crude mitochondria fractions or total homogenates of brain and SPC from SOD1^{G93A} mice at the indicated ages relative to NTg control average (set at 100%; dotted line). The columns represent the mean ± SD. Brain: $n = 4$ (P60), $n = 3$ (P90); SPC: $n = 3$ (P60), $n = 3$ (P90). **c** Hexokinase (HK) activity in total homogenates from hMNs^{A4V} at the indicated days in vitro (DIV) relative to WT control average (set at 100%; dotted line). The columns represent the mean ± SD; $n = 4$ (DIV2), $n = 3$ (DIV7) $n = 3$ (DIV14). **d** Pyruvate dehydrogenase complex (PDHC) activity in total homogenates from hMNs^{A4V} at the indicated (DIV) relative to WT control average (set at 100%; dotted line). The columns represent the mean ± SD; $n = 3$ (DIV7), $n = 3$ (DIV14). **e** Lactate dehydrogenase (LDH) activity in hMNs^{A4V} compared to WT controls. The columns represent the mean ± SE; $n = 3$. **f** CPT1 activity in hMNs^{A4V} relative to WT controls (set at 100%; dotted line). The columns represent the mean ± SD; $n = 3$ (DIV2), $n = 4$ (DIV7), $n = 3$ (DIV14). **g** CPT1 activity in crude mitochondria fractions from the brain (left panel) and SPC (right panel) at the indicated ages relative to NTg control average (set at 100%; dotted line). The columns represent the mean ± SD. Brain: $n = 3$ (P15), $n = 4$ (P30), $n = 4$ (P60); SPC: $n = 4$ (P15), $n = 4$ (P30), $n = 4$ (P60). Data at 120 days in brain and SPC is representative of one experiment using 3 technical replicates from 3 mice in each group. **h** Lipidomics analysis in SOD1^{G93A} mouse tissues (P60) and hMNs^{A4V} (DIV14). Heat maps show fold changes in the levels of the indicated acylcarnitines (ACs), with significant fold changes ($p<0.05$) indicated with asterisks. This increase in C_{14}-C_{18} ACs is more evident in brain mitochondria from SOD1^{G93A} mice (P60) compared to NTg controls. Conversely, these AC species were reduced in SPC mitochondria. Note that shorter ACs (C_2-C_8) were enriched in SPC and hMNs^{A4V}. Data was obtained from 3–5 biological replicates balanced by sex. Colored areas indicate statistical significance ($p<0.05$); Student's two-tailed t-test at an $\alpha = 0.05$ significance level.

https://doi.org/10.1038/s41467-024-51578-1

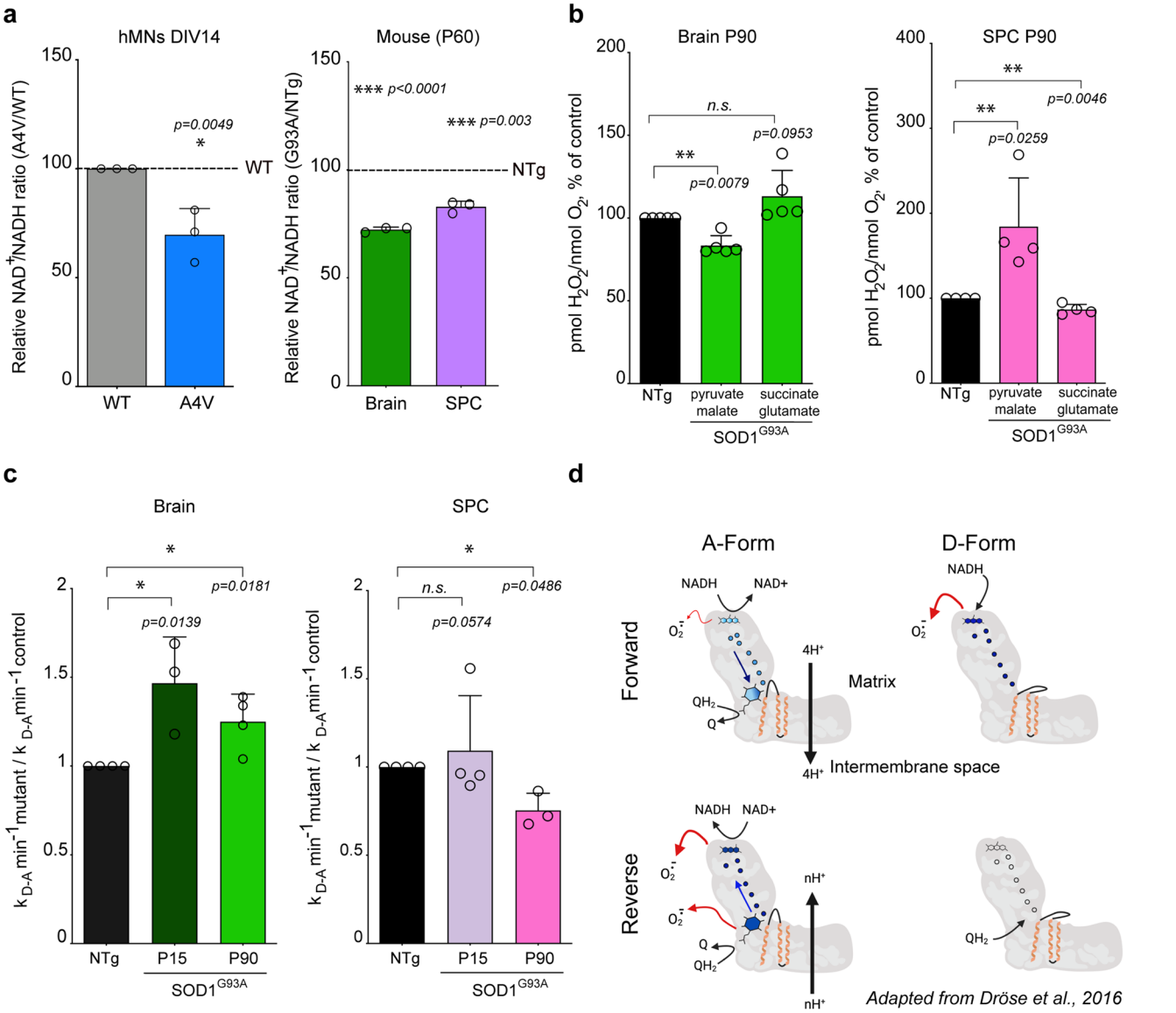

Fig. 4 | Defects in NADH levels and complex I activation in mitochondria from SOD1^{G93A} mice. a NAD$^+$:NADH ratio in hMNs^{A4V} at DIV14 relative to WT control average (set at 100%; dotted line) and SPC at P60 relative to NTg controls (set at 100%; dotted line). The columns represent the mean ± SD; $n = 3$ biologically independent samples. **b** Quantification of hydrogen peroxide (H_2O_2) produced during the oxidation of different substrates in mitochondria from SOD1^{G93A} mice relative to NTg controls (set at 100%; dotted line). The columns represent mean ± SD; brain: $n = 4$, SPC: $n = 4$. **c** Analysis of the D-to-A transition constant for CI, calculated and expressed as min^{-1} (see Supplementary Fig. 3 for absolute values). The data are shown as the values in SOD1^{G93A} mice relative to NTg (set at 1). The columns represent the mean ± SD; brain: $n = 3$ (P15), $n = 4$ (P90); SPC: $n = 4$ (P15), $n = 3$ (P90). **d** Schematical representations of Complex I conformational changes during forward and reverse electron transfer (Created with BioRender released under a Creative Commons Attribution-NonCommercial-NoDerivatives 4.0 International License, OE26XW1WA2). Statistical test: Student's two-tailed t-test for normal data or the Mann-Whitney U test for non-normal data at an $\alpha = 0.05$ significance level. Statistical significance is shown as: n.s. $p>0.05$; * $p<0.05$; ** $p<0.01$; *** $p<0.001$; **** $p<0.0001$.

proteins[24]. Alterations in the lipid composition of MAM domains impair the enzymatic activities of the proteins that are localized within these ER regions[58,59]. Thus, to validate our functional data, we conducted lipidomics analysis of total homogenates and subcellular fractions from brain and SPC tissues from SOD1^{G93A} mice, as well as in postmortem ALS brain sections (Fig. 6). This analysis revealed a significant reduction in the steady-state levels of free cholesterol (FC) and sphingomyelin (SM) in MAM fractions from SOD1^{G93A} mouse SPC and a concomitant increase in these two lipid classes in the ER, whereas only brain total homogenates showed an alteration in SM levels at presymptomatic stages (P60) (Fig. 6a, b). Similarly, the distribution of FC and SM was reduced in the postmortem sALS patient and SOD1^{G93A} mouse brain, with significantly lower levels of these two lipid classes specifically in MAM fractions (Fig. 6c, d). Lipidomics data also revealed alterations in specific phospholipid species in MAM fractions from human and mouse mutant tissues, particularly in species with long and polyunsaturated FAs (Supplementary Fig. 5a–d). Furthermore, MAM fractions from human ALS brain samples also showed an imbalance in the levels of phosphatidylserine (PtdSer) species towards an increase in those bound to unsaturated FAs (Supplementary Fig. 5e). Overall, our data indicate that the distinctive lipid-raft milieu of MAM domains is disturbed in ALS tissues in line with the defects we observed in the enzymatic activities regulated at these ER regions.

To understand how mutations in *SOD1* affect the protein architecture of MAM domains, we conducted proteomics analysis of MAM fractions from cellular models. To obtain the necessary material to

https://doi.org/10.1038/s41467-024-51578-1

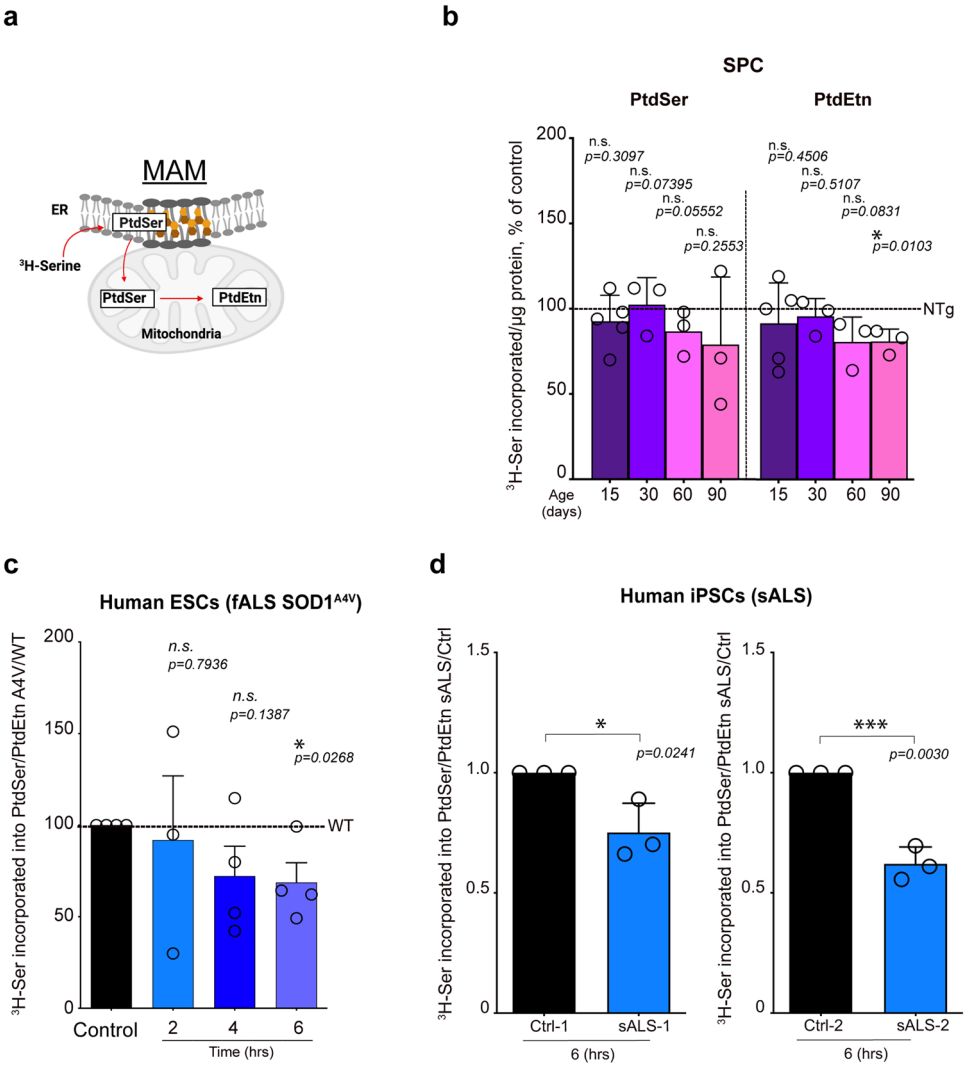

Fig. 5 | Downregulation of MAM activity in familial and sporadic models of ALS. **a** Scheme of MAM domains formed between the ER and mitochondria, showing the phospholipid synthesis and transfer assay (Created with BioRender released under a Creative Commons Attribution-NonCommercial-NoDerivatives 4.0 International License, WN26XW044I). **b** Quantification of MAM activity by the synthesis and transfer of phospholipids between the ER and mitochondria in crude mitochondria fractions from SOD1^{G93A} mouse SPC at the indicated ages. The columns represent the mean of PtdSer and PtdEtn content/µg crude mitochondria ± SD relative to controls (set at 100%; dotted line). $n = 5$ (P15), $n = 3$ (P30), $n = 3$ (P60), $n = 3$ (P90) biologically independent samples. **c** MAM activity via the phospholipid synthesis and transfer assay in hMNs^{A4V} (DIV14) at 2, 4, and 6 h. The columns represent the mean of the PtdEtn/PtdSer ratio of ALS vs WT controls (black bars set at 100%; dotted line). $n = 3$ (2 h), $n = 4$ (4 h), $n = 4$ (6 h). **d** MAM activity via the phospholipid synthesis and transfer assay at 6 h in iPSCs from sALS patients: Ctrl-1/sALS-1 and Ctrl-2/sALS-2 (see Supplementary Information for additional details about these samples). The columns represent the mean of the PtdEtn/PtdSer ratio of sALS vs healthy controls (black bars set at 1; dotted line); $n = 3$. Statistical test: Student's two-tailed t-test at an $\alpha = 0.05$ significance level. Statistical significance is shown as: n.s. $p>0.05$; * $p<0.05$; ** $p<0.01$; *** $p<0.001$; **** $p<0.0001$.

perform these assays, we transfected NSC-34 cells with plasmids encoding human SOD1^{WT} or SOD1^{G93A}, with non-transfected cells as a control (Supplementary Fig. 6a). We analyzed the protein composition of total homogenates and MAM fractions using a PhotoClick-cholesterol approach, as described[60] (Fig. 7a). Briefly, PhotoClick-cholesterol proteomics enables untargeted identification of cholesterol-interacting proteins, with analyses in cholesterol-enriched lipid raft fractions (such as MAM) indicating which proteins are most abundant in those domains. After treating cells with PhotoClick-cholesterol, a *trans*-sterol lipid probe that acts as a cholesterol analog, we immunoprecipitated UV-crosslinked (via Click chemistry) cholesterol-interacting proteins from MAM fractions. In line with our data from the functional assays, we found that cells overexpressing SOD1^{G93A} showed reductions in the levels of MAM-specific proteins, such as ER lipid raft associated 2 (Erlin2), oxysterol-binding protein like-8 (Osbpl8), acyl-CoA:cholesterol acyltransferase-1 (Acat1), acyl-CoA synthase long chain 4 (Acsl4), and neutral sphingomyelinase 2 (nSMase2/Smpd3) (Fig. 7b).

As shown previously in other disease models[54,61], our proteomics analyses here in the context of ALS revealed that MAM fractions from SOD1^{G93A} cells showed significantly reduced levels of enzymes comprising the glycolytic pathway relative to control cells (Fig. 7b). We also found reduced levels of these enzymes in SOD1^{WT} cells. Only triose-phosphate isomerase 1 (Tpi1) showed higher levels in MAM from SOD1^{G93A} and SOD1^{WT} cells. Parallel to reductions in most glycolytic enzymes, MAM fractions from these cells displayed higher levels of enzymes involved in maintaining energy production during low-glucose conditions, such as glycerol-3-phosphate dehydrogenase (Gpd2), hydroxy-3-methylglutaryl-CoA lyase (Hmgcl), and 3-ketoacyl-CoA thiolase A (Acaa1a). In addition, *SOD1* we found significant increases in proteins involved in the oxidative stress response at the MAM, such as peroxiredoxins (Prdx1 and Prdx5) and heat-shock

https://doi.org/10.1038/s41467-024-51578-1

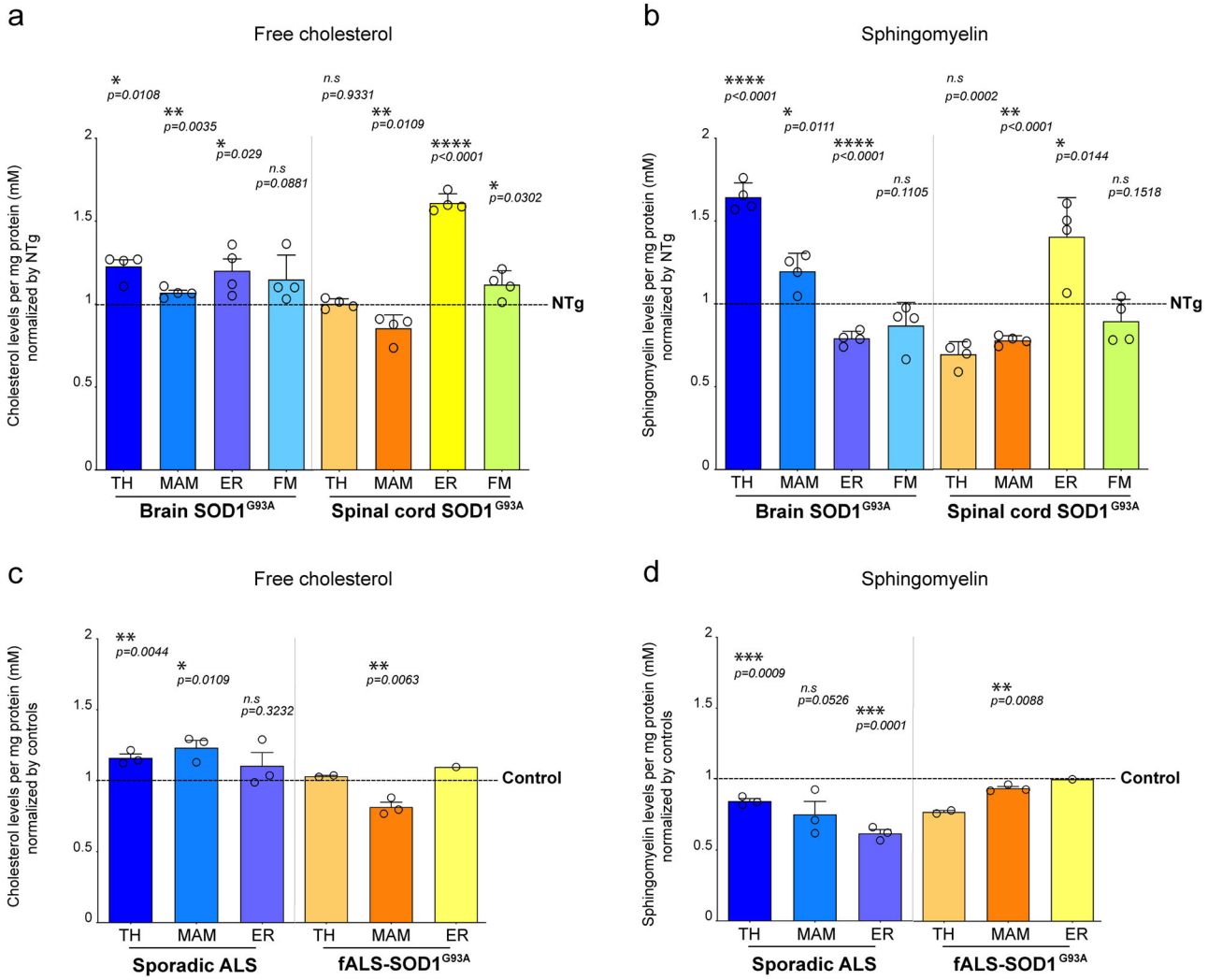

Fig. 6 | Lipidomics analysis of mouse and human ALS tissues. a, **b** Quantification of cholesterol and sphingomyelin levels in subcellular fractions from SOD1^{G93A} mouse brain and SPC tissues at pre-symptomatic stage P60 and in **c**, **d** postmortem frontal cortex samples from sALS and fALS patients with mutations in *SOD1* (SOD1^{G93A}). In mouse samples, data are shown as the mean ± SD of $n = 4$ biologically independent samples balanced by sex. For human samples, data are shown as mean from 3–5 replicates consisting of a pool of tissues from 2 fALS cases with SOD1^{G93A} and 3 sALS cases (balanced by sex) normalized to control values ± SE. See Supplementary Information for additional details about these tissues. Statistical test: Student's two-tailed *t*-test at an $\alpha = 0.05$ significance level. Statistical significance is shown as: n.s. $p>0.05$; * $p<0.05$; ** $p<0.01$; *** $p<0.001$; **** $p<0.0001$.

protein 90 b1 (Hsp90b1) (Fig. 7b). We also found that MAM from SOD1^{WT} cells showed higher levels of ALS-related proteins, such as TAR DNA-binding protein (Tdp43), fused-in-sarcoma (Fus), ataxin 2 (Atxn2), valosin containing protein (Vcp), and Sod1 itself, compared to non-transfected cells (Supplementary Fig. 7a). SOD1^{G93A} cells also showed increases in many of these proteins. Therefore, our results provide validation that MAM formation recruits key enzymes involved in the regulation of glycolysis and that mutations in *SOD1* can impair this localization.

Previous reports[28] and our own data (Supplementary Fig. 6b) have shown that SOD1 is present in MAM domains. Therefore, we measured potential SOD1 interactors at MAM by proximity-dependent biotin labeling in NSC-34 cells overexpressing myc-BioID2-SOD1^{WT} or myc-BioID2-SOD1^{G93A} [62] (Supplementary Fig. 6c). Our data showed that myc-BioID2-SOD1^{WT} labeled MAM-resident proteins, including Erlin2 and Acat1 (Fig. 7c). We also detected positive interactions between SOD1^{WT} and many of the glycolytic enzymes detected at MAM via the PhotoClick-cholesterol studies above, and these interactions were reduced with mutant SOD1 (Fig. 7c). On the other hand, compared to SOD1^{WT}, we detected an increase in positive interactions between SOD1^{G93A} and proteins involved in the regulation of metabolic adaptation and oxidative stress (Fig. 7c). We also note that, apart from labeling Sod1 itself, myc-BioID2-SOD1^{G93A} was more efficient in labeling ALS-associated protein, Atxn2, at MAM compared to SOD1^{WT} (Supplementary Fig. 7b). Altogether, our PhotoClick-cholesterol and BioID2 proteomics results led us to conclude that mutations in *SOD1* induce significant alterations in the structure of MAM. This resulted in reduced levels of glycolytic enzymes and increased levels of metabolic adaptation and oxidative stress proteins at MAM.

To better understand the impact of MAM defects on the alterations in glucose and pyruvate metabolism observed in ALS samples, we exploited the lipid-raft nature of these domains by inducing their formation in cultured hMNs. MAM formation in the ER is known to be triggered by local elevations in cholesterol delivered from the plasma membrane (PM)[60]. Cholesterol mobilization has long been known to be stimulated by the activation of cellular sphingomyelinases (SMases) and can be replicated by incubation with exogenously added SMase[63]. Therefore, we induced cholesterol trafficking from the PM to the ER (thus inducing the formation of MAM) by incubating hMNs^{A4V} and WT controls with SMase from *Bacillus cereus*, as described previously[63,64].

https://doi.org/10.1038/s41467-024-51578-1

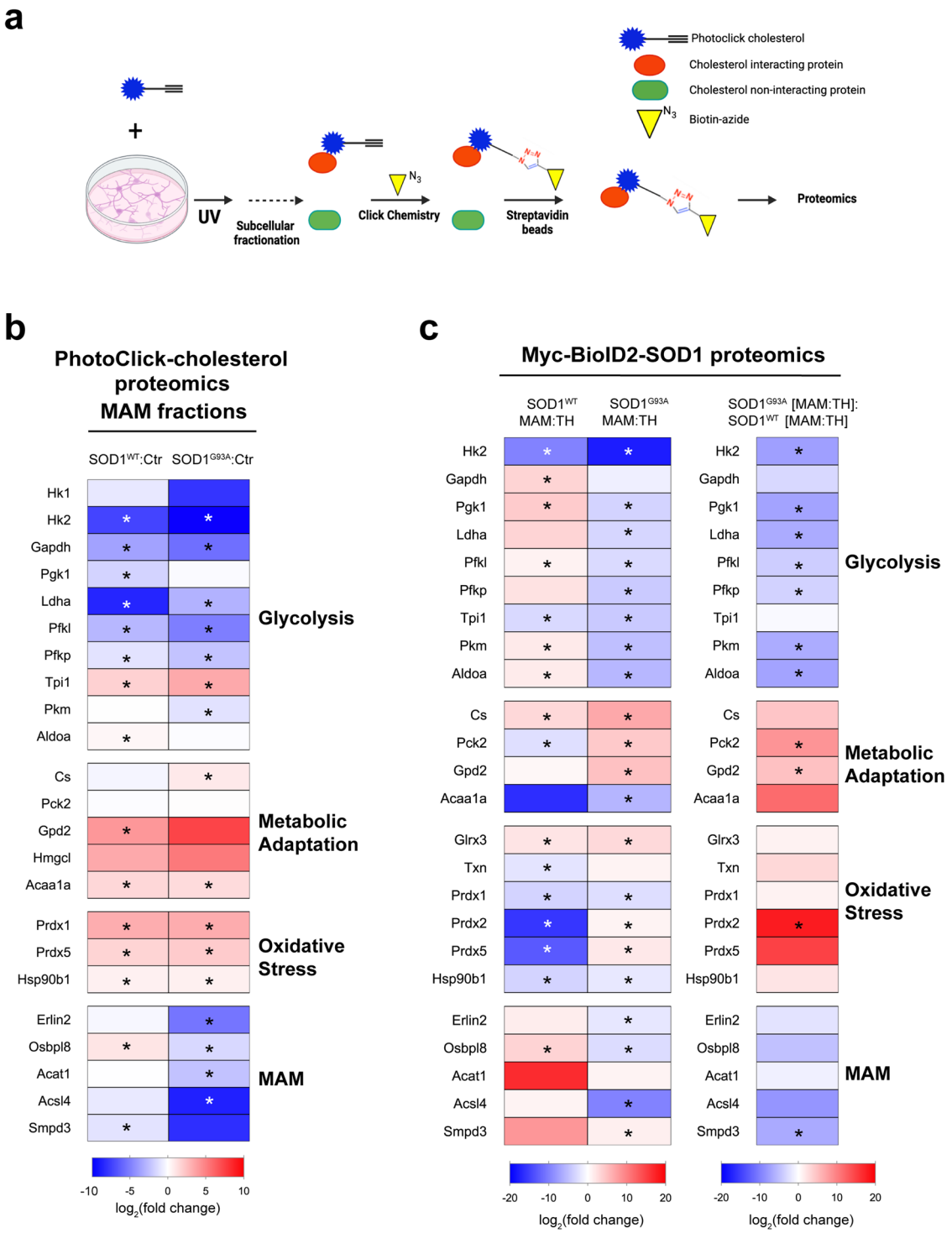

Fig. 7 | Proteomics changes in MAM fractions from NSC-34 cells expressing mutant *SOD1*. **a** Scheme of PhotoClick-cholesterol methodology. **b** Proteomics analysis of the PhotoClick-cholesterol interactome in MAM fractions from NSC-34 cells expressing either $SOD1^{WT}$ or $SOD1^{G93A}$. Heat maps show fold changes in the indicated proteins compared to non-transfected controls (Ctr), with statistically significant ($p<0.05$) fold changes indicated with asterisks. **c** Proteomics analysis of biotinylated proteins from cells expressing either myc-BioID2-$SOD1^{WT}$ or myc-BioID2-$SOD1^{G93A}$. Left: spectral counts for the indicated proteins from MAM fractions are shown normalized to TH values for both SOD1 mutants. Right: the normalized MAM values from $SOD1^{G93A}$ are normalized to the normalized MAM values from $SOD1^{WT}$. For all heat maps in this figure, the results show the mean of $n = 3$ biologically independent samples (colored areas indicate statistically significant fold changes; $p<0.05$, Student's two-tailed t-test at an $\alpha = 0.05$ significance level); red indicates increases and blue indicates decreases. Glycolytic enzymes: hexokinase-1 and -2 (Hk1, Hk2); glyceraldehyde 3-phosphate dehydrogenase (Gapdh); phosphoglycerate kinase (Pgk1); lactate dehydrogenase A (Ldha); phosphofructokinase (Pfkl, Pfkp); triose-phosphate isomerase 1 (Tpi1); pyruvate kinase isoform M (Pkm); fructose-bisphosphate aldolase A (Aldoa). Enzymes involved in metabolic adaptation: citrate synthase (Cs); phosphoenolpyruvate carboxykinase 2 (Pck2); glycerol-3-phosphate dehydrogenase (Gpd2); hydroxy-3-methylglutaryl-CoA lyase (Hmgcl); 3-ketoacyl-CoA thiolase A (Acaa1a). Proteins involved in oxidative stress: glutaredoxin-3 (Glrx3); thioredoxin (Txn); peroxiredoxins (Prdx1, 2 and 5); heat-shock protein 90 b1 (Hsp90b1). MAM-resident proteins: ER lipid raft associated 2 (Erlin2); oxysterol-binding protein like-8 (Osbpl8); acyl-CoA:cholesterol acyltransferase-1 (Acat1); acyl-CoA synthase long chain 4 (Acsl4); neutral sphingomyelinase 2 (nSMase2/Smpd3).

https://doi.org/10.1038/s41467-024-51578-1

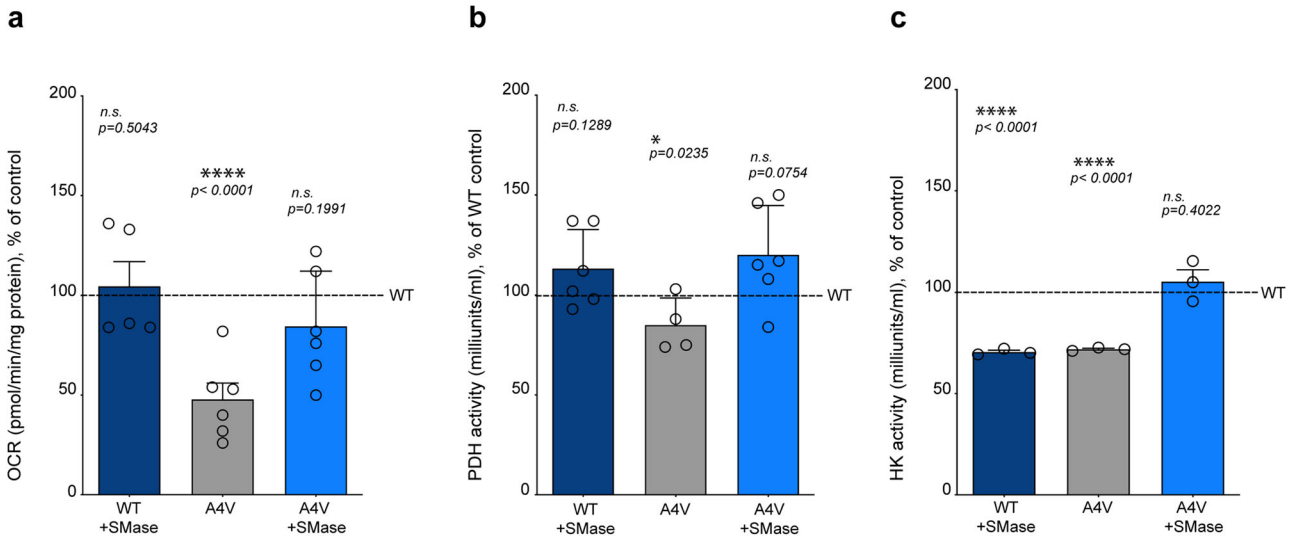

Fig. 8 | Stimulation of MAM formation reverses mitochondrial phenotypes in ALS motor neurons. a Quantification of OCR in hMNs^{A4V} using pyruvate as a mitochondrial substrate before and after SMase treatment compared to untreated WT cells (set at 100%). Data are shown as mean ± SD of $n = 6$ biologically independent samples. **b** PDHC activity in hMNs^{A4V} before and after SMase treatment compared to untreated WT cells (set at 100%). Data are shown as mean ± SD; $n = 3$. **c** HK activity in hMNs^{A4V} before and after SMase treatment compared to untreated WT cells (set at 100%). Data are shown as mean ± SE; $n = 3$. Statistical test: Student's two-tailed t-test at an $\alpha = 0.05$ significance level. Statistical significance is shown as: n.s. $p>0.05$; * $p<0.05$; ** $p<0.01$; *** $p<0.001$; **** $p<0.0001$.

As expected, SMase treatment stimulated the internalization of cholesterol (determined by increased filipin staining) as well as the formation and activation of MAM domains (Supplementary Fig. 8a–d). Notably, treatment of hMNs^{A4V} with SMase rescued previously observed defects in NADH-CI-driven OCR, PDHC and HK activities (Fig. 8), and the mRNA expression of *MFN2* compared to non-treated WT cells (Supplementary Fig. 8e). The restoration of PDHC activity is consistent with a reduction in CPT1 activity, which would decrease FA import into mitochondria (Supplementary Fig. 8f). These results imply that MAM dysfunction contributes to the impairment of pyruvate metabolism and the subsequent shift in mitochondrial fuels in ALS models.

Taken together, our data underscores the essential role of MAM in the regulation of cellular metabolism, and points to its dysfunction in ALS as a potential source of the bioenergetic defects characteristic of this devastating disease.

Discussion

In support of previous reports[28,25], our results show that ER-mitochondria communication and MAM functionality are diminished in cells with mutations in *SOD1* and other ALS genes. We also found that *SOD1*-mutant cells undergo alterations in the lipid structure and protein composition of their MAM domains, along with reductions in the expression of the ER-mitochondria tether, MFN2. Our data thus agree with previous evidence of MAM defects in the context of mutations in genes other than *SOD1*, such as *SIGMAR1*, *TARDBP*, and *FUS*[28,65]. Moreover, we show here that sALS cells also display disturbances in MAM, implying that these alterations could be common and relevant to all forms of the disease.

In *SOD1*-mutant cells, we show that the dysfunction of MAM impairs pyruvate metabolism and its use as a mitochondrial fuel source, which in turn induces a shift towards the use of FAs as an alternative substrate for ATP production. We posit that, when prolonged over time, this shift contributes to the mitochondrial respiratory defects characteristic of ALS cells.

Our results indicate that bioenergetic defects in SPC tissues from *SOD1*-mutant mice appear earlier than in the brain and are also more severe, in agreement with the progression of the disease. The reason behind these differences remains unknown. One possibility is that the high energetic demands of MNs render the SPC more sensitive to the loss of metabolic flexibility caused by a progressive dysfunction in MAM domains, compared to other cell types and areas of the CNS.

Alterations in pyruvate and mitochondrial metabolism were reversed by stimulating the formation of MAM domains in mutant cells, which led us to conclude that the bioenergetic defects in these ALS models, and perhaps in other forms of ALS, are downstream consequences of a prior impairment in the regulation of MAM. In agreement, stimulating the expression of known ER-mitochondria tethers, such as MFN2, was able to rescue mitochondrial abnormalities in fALS models with mutations in *TARDBP*[66]. While further research is needed, these results validate the seminal role of MAM in the cascade of events underlying the regulation of bioenergetics.

Relevant to this, several reports have shown that, in addition to its role in lipid homeostasis and calcium regulation, MAM is an essential locus for the regulation of glucose metabolism and metabolic flexibility[23,67]. Specifically, MAM integrity was shown to be essential for insulin and glucagon signaling via the modulation of hexokinase 2[54]. Furthermore, the dysfunction of ER-mitochondria contacts and MAM domains was shown to be associated with impairments in pyruvate metabolism and insulin resistance, and increased MAM formation improved glucose tolerance[23,68]. In agreement with these data, our proteomics analysis revealed that several glycolytic enzymes can be localized to MAM. The relevance of this localization to the regulation of glucose oxidation requires further investigation. Nevertheless, our proteomics results support the idea that the formation of MAM could facilitate the compartmentalization of pyruvate production in areas close to mitochondria. In line with this idea, our work shows that *SOD1*-mutant cells display impaired MAM formation and a reduced number of glycolytic enzymes in these ER domains adjacent to mitochondria. Our BioID2 results also suggest that SOD1 is localized to MAM and is in close proximity to specific glycolytic enzymes. However, this proximity labeling data does not necessarily reflect physical or functional interaction of these glycolytic enzymes with SOD1; rather, their close association with SOD1 may be the result of spatial convergence when MAM is formed.

Limitations in pyruvate availability in *SOD1* mutants shift mitochondrial metabolism towards the use of other carbon sources for ATP

production, such as FAs, which could help explain some of the phenotypes characteristic of ALS patients. For instance, this shift in mitochondrial fuels is consistent with the mobilization of FAs from triglyceride stores and with alterations in glucose metabolism, including insulin resistance, observable in ALS patients[8,69–71] and mouse models[45]. Moreover, the decreased production and use of pyruvate as a mitochondrial fuel could explain the high levels of lactate (and glucose) in the blood of ALS patients[8] and the low NAD^+:NADH ratio found in our ALS models. Under these conditions, non-oxidized glucose can be channeled through alternative, non-ATP-producing pathways, such as the formation of advanced glycation end products, the synthesis of hexosamine, and astrocytic storage of glycogen, all of which are upregulated in ALS[7,72]. Finally, a shift towards the use of FAs could also underlie the imbalance in lipoprotein levels found in blood and tissue samples from ALS patients[70,73], and the observation that high-fat diets improve ATP levels and slow disease progression in ALS cases[74].

Persistent use of FAs (and amino acids) for ATP production can alter the flow of electrons in mitochondrial respiratory complexes and boost the levels of reduced CoQ ($CoQH_2$), inducing RET and the reversal of CI activity, alongside higher levels of NADH and superoxide[49]. It has been proposed that RET is triggered in mitochondria under nutrient stress as a mechanism to maintain membrane potential and NADH levels, to fuel those respiratory complexes working in the forward direction[75]. Our results confirm that *SOD1*-mutant cells and tissues display phenotypes consistent with the induction of RET in mitochondria, which could help explain why ALS cells, despite displaying significant decreases in mitochondrial respiration, have higher membrane potential values compared to controls[4,76].

A critical finding that arises from our studies is that metabolic disturbances in the disease are dynamic and progressive and should, therefore, be analyzed longitudinally. In healthy cells, induction of RET allows the cell to adapt the structure and function of respiratory complexes to low-glucose conditions[42]. However, when prolonged over time, RET results in the loss of mitochondrial metabolic flexibility, bioenergetic defects, and oxidative damage[43,51]. Previous studies have shown that CI, when working in reverse, induces an increase in superoxide (O_2^-) production and subsequent elevations in *SOD1* expression and H_2O_2 levels[77,78]. These phenotypes have been previously observed in the context of familial and sporadic ALS[79]. Elevations in H_2O_2 can induce the expression of hypoxia-inducing factor 1a (*HIF1A*)[80]. Therefore, sustained RET activation could help explain the development of pseudo-hypoxic phenotypes in the disease and the increased expression of HIF1A target genes in ALS models[81].

Nutritional state and hypoxic stress can cause the conversion of CI to the deactivated or D-form[16,51]. Although this conformational change is physiologically reversible, prolonged exposure to oxidative stress under RET can irreversibly deactivate CI[10,19]. Our data show a significant delay in CI activation in SPC mitochondria from $SOD1^{G93A}$ mice, which suggests that there is a larger pool of inactive CI in this tissue compared to brain samples and controls. In agreement with our results, it is proposed that this conversion of CI from the A to the D form alters the conformation of its structure, impeding the flow of electrons from NADH (i.e., forward mode) and diverting these electrons into the mitochondrial matrix, thereby stimulating the formation of O_2^-. Note that the electrons transferred in a reverse direction from $CoQH_2$ to CI in the D-form do not elicit ROS production[19] because, when CI is in the D-form, electrons do not have access to the ubiquinone-binding site (Fig. 4d). Finally, in its D-form, CI is also more susceptible to covalent modifications, such as nitrosylation and oxidation[82], both of which are well-known contributors to ALS pathogenesis[83]. Altogether, we propose that, during the progression of ALS, CI deactivation becomes irreversible, in support of the

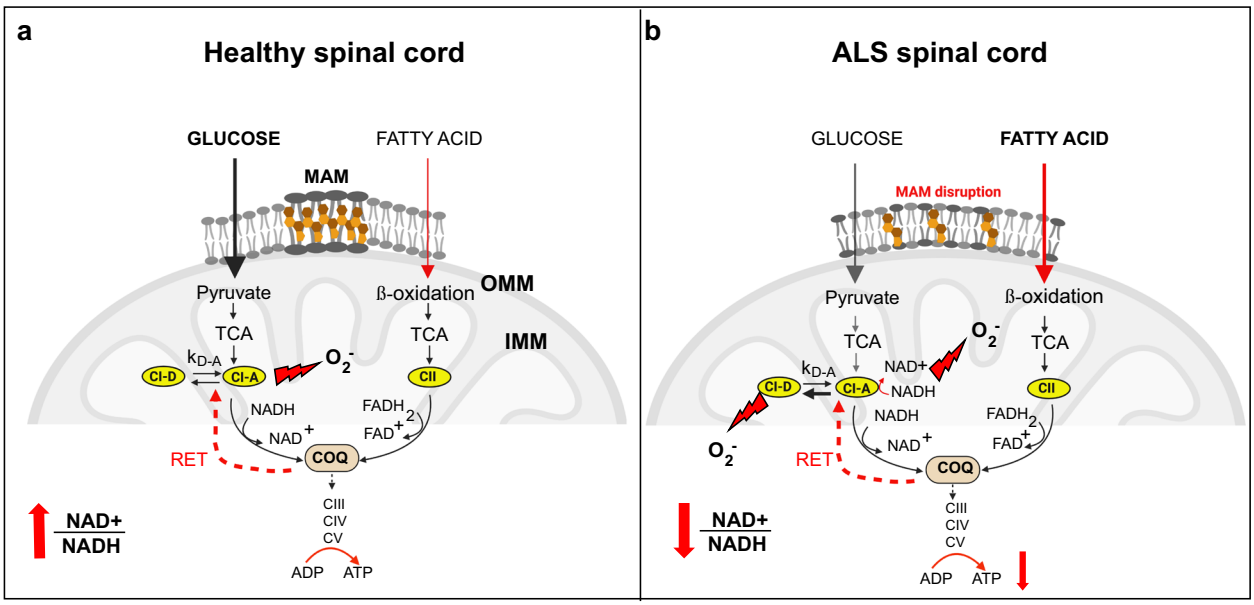

Fig. 9 | Model of mitochondrial metabolic dysfunction in ALS. MAM down-regulation shifts mitochondrial metabolism and precedes mitochondrial defects in *SOD1*-mutant models. **a** In healthy neurons, mitochondria associate with the ER, promoting pyruvate metabolism and NADH-driven oxygen consumption with relatively low ROS generation. Note that the cell maintains a high NAD^+:NADH ratio to sustain the continuous production of NADH to fuel ATP production, and maintain CI working in forward mode. **b** In contrast, in the SPC of ALS mice, the dysfunction of MAM hinders pyruvate metabolism and induces a shift from pyruvate to other carbon sources such as FAs, promoting increases in succinate and $FADH_2$-driven respiration, and the transfer of electrons from CII to CoQ. Over time, this surge in FA oxidation increases the pool of reduced CoQ, triggering RET and subsequently higher levels of ROS. The radicals generated in this process differentially affect the kinetics of CI activation in SPC compared to the brain (Fig. S6). In this scenario, the SPC displays a low NAD^+:NADH ratio (Created with BioRender released under a Creative Commons Attribution-NonCommercial-NoDerivatives 4.0 International License, HZ26XVZMOD).

frequently reported impairments in CI activity in models of the disease[3,84]. However, we posit that rather than being *defective*, CI is *inactivated* in our ALS models.

One open question in the current study is why the delay in CI inactivation was detected only in SOD1^{G93A} SPC mitochondria but not in the brain. Our results show that, despite displaying increased FA oxidation, the brain maintains a higher pool of active CI in mutants compared to controls. It is possible that the different metabolic phenotypes observed in the brain and SPC under the same metabolic constraints can be the result of tissue-specific regulation of NAD^+ pathways. Intriguingly, previous evidence has demonstrated that MNs are particularly sensitive to changes in NAD^+:NADH ratios and that reductions in NAD^+ could be a common phenomenon in MN disorders[85].

Our findings lead us to propose the following model of ALS pathogenesis. In a healthy neuron, the formation of MAM domains favors pyruvate metabolism and NADH-fueled respiration via CI, with relatively low ROS generation (Fig. 9a). In this scenario, the cell maintains high NAD^+:NADH and NADH:$FADH_2$ ratios. In contrast, in ALS cells, an initial dysfunction of MAM would impair pyruvate production and induce a shift to FA β-oxidation which, in turn, would stimulate succinate-mediated mitochondrial respiration and increase $CoQH_2$ levels. In this scenario, RET is triggered, resulting in high levels of ROS production by CI (Fig. 9b). If RET conditions persist in the ALS cell, CI would progressively adopt a deactivated conformation to avoid significant oxidative damage[10,19]. Over time, these metabolic disturbances would raise NADH levels, favoring pyruvate usage and indirectly inhibiting CPT1, promoting incomplete FA oxidation and increased production of short AC species in mutant SPC tissues[20]. We hypothesize that these metabolic alterations progressively outweigh the cell's capacity to buffer them, and ultimately contribute to cell and tissue dysfunction in ALS.

Taken together, our data implicate disrupted ER-mitochondria communication at MAM domains as a crucial event in the pathogenesis of ALS and a critical mediator of metabolic and mitochondrial defects in this devastating disorder.

Methods

This research complies with all relevant ethical regulations. All animal husbandry and experimentation were conducted in accordance with the National Institutes of Health Guide for Care and Use of Laboratory Animals. Mice were housed under a 12-hour light/dark cycle, and vivarium ambient temperature and humidity were maintained as per recommendations in the Guide. All procedures were approved by the Columbia University Institutional Animal Care and Use Committee (protocol AC-AABK5603), the New York Brain Bank (NYBB) at Columbia University (RRID: SCR_007142; RRID: nlx_43593), and Comité Coordinador de Ética de la Investigación Biosanitaria de Andalucía (CCEIBA).

Animal and cell models

hSOD1 transgenic mice: Here, we used B6SJL-Tg (SOD1*G93A)1Gur/J mice (strain 002726) that have a high transgene copy number of the G93A-mutated hSOD1, and age-matched non-transgenics (NTg), from Jackson Laboratories. Genotypes were verified by PCR of tail DNA using the RedExtract-N-Amp™ Tissue PCR Kit (MilliporeSigma XNAT). G93A mice began exhibiting paralytic symptoms at 90 days of age and had mean lifespans of 120–130d. For biochemical and transcriptional assays, animals were sacrificed by decapitation at post-natal day 15 (P15), 30 (P30), 60 (P60), 90 (P90), or 120 (P120). For mitochondrial and enzymatic assays, brain and spinal cord (SPC) tissues were removed immediately, washed in cold 1X phosphate-buffered saline (PBS, Fisher Scientific SH3002802), and either homogenized (described below) or snap-frozen in liquid nitrogen. For all studies, each experimental sample consisted of pooled tissues from at least two mice at a female/male ratio of 1:1. At least three technical replicates per group were assayed in every experiment, and every experiment was repeated at least 3 times for 3 biological replicates.

Human and mouse embryonic stem cell (ESC)- and human induced pluripotent stem cell (iPSC)-derived SPC motor neurons (MNs): For hESCs, we used the SOD1$^{+/A4V}$ and SOD1$^{+/+}$ isogenic cell lines described previously[86]. These cells were generated in the HuES 3 *Hb9*::GFP cell line and are extensively described in ref. 87. We also used mESCs derived from hSOD1^{WT} or hSOD1^{G93A} transgenic mice expressing EGFP under the control of a MN-specific promoter[86]. We also differentiated MNs from iPSCs derived from sALS patients. All cell lines used in this work are listed in Supplementary Table 2. The ESCs and iPSCs were maintained in mTeSR1 Plus Medium (Stemcell Technologies 100-0276) containing 1 μM Rock inhibitor (RI) (Tocris 1254) in plates coated with Matrigel (Corning 354230).

Differentiation of human SPC MNs was performed as described[86] with modifications over a course of 16 days. One million cells were seeded into an ultra-low attachment plate (Corning 4615) containing a final volume of 12 mL N2/B-27 media: a 1:1 ratio of Advanced DMEM/F12 medium (ThermoFisher Scientific 12634028) containing N2 supplement (ThermoFisher Scientific 17502048), and Neurobasal medium (ThermoFisher Scientific 21103049) containing B-27 supplement (without Vitamin A; ThermoFisher Scientific 12587010), with 25 μM ß-mercaptoethanol (ThermoFisher Scientific 21985023) and standard concentrations of penicillin/streptomycin (pen/strep; ThermoFisher Scientific 15140122) and L-glutamine (ThermoFisher Scientific A2916801). Supplementation of N2/B-27 media with various factors was done as follows. **Day 0:** 10 ng/mL recombinant human FGF basic/FGF2/bFGF (146 aa) protein (R&D Systems 233-FB), 10 μM RI, 20 μM SB431542 (Stemcell Technologies 72234), 0.1 μM LDN-193189 (Stemgent 04-0074-02), 3 μM CHIR 99021 (Tocris 4423/10) and 10 μM ascorbic acid (AA) (Stemcell Technologies 72132). **Day 2:** 20 μM SB431542, 0.1 μM LDN-193189, 3 μM CHIR 99021, 10 μM AA, 100 nM retinoic acid (RA) (Tocris 1254) and 500 nM Smoothened Agonist (SAG; Stemcell Technologies 73414). **Day 4:** 20 μM SB431542, 0.1 μM LDN-193189, 10 μM AA, 100 nM RA, and 500 nM SAG. **Day 7:** 10 μM AA, 100 nM RA and 500 nM SAG. **Day 9:** 10 μM AA, 100 nM RA, 500 nM SAG, and 10 μM γ-secretase inhibitor (DAPT, R&D Systems 2634/10). **Day 11:** 10 μM AA, 100 nM RA, 500 nM SAG, 10 ng/mL recombinant human brain-derived neurotrophic factor (BDNF, R&D Systems 248-BDB-005), and 10 μM DAPT. **Day 14:** 10 μM AA, 100 nM RA, 10 ng/mL BDNF, 10 μM DAPT, and 10 ng/mL glial cell-derived neurotrophic factor (GDNF, R&D Systems 212-GD). Cells (embryonic bodies, EBs) were dissociated on **day 16**. Briefly, EBs were collected in a 50 mL tube, washed with PBS (containing Ca^{2+}/Mg^{2+}), and incubated with 1 volume of 0.25% trypsin-EDTA (ThermoFisher Scientific 25200114) supplemented with DNase (Worthington Biochemical Corporation LK003172) for 15 min (vortexing every 5 min) in a water bath at 37 °C. Trypsinization was stopped by adding 2 volumes of 10% fetal bovine serum (FBS, MilliporeSigma F2442). The cells were collected from the supernatant, filtered through a 40 mm filter (Fisher Scientific 08-771-1), and centrifuged at 200 x *g* for 5 min. The resulting pellet was resuspended in N2/B-27 media with the Day 0 differentiation factors listed above, and the cells were plated on poly-L-lysine (R&D Systems 3438-200-01) and laminin (4 μg/mL, MilliporeSigma L2020) coated surfaces. The cells were differentiated in vitro for 2, 7 or 14 days (unless otherwise indicated) in neuronal differentiation media [Neurobasal medium containing N2 supplement, B-27 supplement with vitamin A (ThermoFisher Scientific 17504044), pen/strep, L-glutamine, non-essential amino acids (NEAA, ThermoFisher Scientific 11140076), 1 μM antimitotic U-FdU (stock 10 mM uridine, MilliporeSigma U3750; stock 10 mM 5-fluoro-2'-deoxyuridine, MilliporeSigma F0503), 10 ng/mL GDNF, 10 ng/mL BDNF, 10 ng/mL ciliary

neurotrophic factor (CNTF, Miltenyi Biotec 130-096-337), 25 μM L-glutamic acid (MilliporeSigma G5889), 25 μM ß-mercaptoethanol, 10 μM forskolin (Stemcell Technologies 72114), and 100 μM 3-isobutyl-1-methylxantine (IBMX, R&D Systems 2845/50)]. All cell lines used were routinely tested for mycoplasma following manufacturer instructions (Genlantis™ MycoScope™ PCR Detection Kit, Fisher Scientific MY01050).

Differentiation of transgenic mouse ESCs (hSOD1^{WT} or hSOD1^{G93A}) was performed as previously described[86]. Briefly, cells were dissociated on day 6 of differentiation and plated on a surface coated with polyornithine (100 μg/mL, MilliporeSigma P4957) and laminin (4 μg/mL). Cells were cultured in the presence of the cAMP-elevating compounds forskolin (10 mM) and IBMX (100 mM) in combination with 500 mM GDNF.

Primary patient fibroblasts: Primary fibroblasts from fALS patients (carrying mutations in *SOD1* or *FUS*), sALS patients, and healthy controls were grown in DMEM (ThermoFisher Scientific 11965092) supplemented with 10% FBS and pen/strep (Supplementary table 2). For sALS patient fibroblasts, the culture protocols were approved by the Comité Coordinador de Ética de la Investigación Biosanitaria de Andalucía (CCEIBA).

Cell lines: NSC-34 cells were maintained in DMEM supplemented with sodium pyruvate (ThermoFisher Scientific 11360070), L-glutamine and 10% FBS. Mouse embryonic fibroblasts and Neuro-2a cells were maintained in DMEM supplemented with 10% FBS and pen/strep.

Human brain samples: Human brain samples were obtained from the New York Brain Bank (NYBB) at Columbia University (RRID: SCR_007142, RRID: nlx_43593). In all cases, we used frontal cortex areas (Supplementary table 3).

Bioenergetics analyses

Crude mitochondria fractions from mouse tissue homogenates: Respirometry of isolated mitochondria from brain and SPC tissue and from cell cultures was performed using the Seahorse XFe24 Extracellular Flux Analyzer (Agilent Technologies). Collection of crude mitochondria fractions and measurement of mitochondrial oxygen consumption rate (OCR) was determined as previously described[59,88]. In summary, mice were sacrificed by decapitation at P15, P30, P60, P90 and P120. The brain and SPC were extracted immediately and washed in cold 1X PBS. Each sample was prepared by pooling tissues from 4 different animals: 2 male and 2 female per genotype. The tissues were homogenized in 10 volumes of homogenization buffer (210 mM mannitol, 70 mM sucrose, 5 mM HEPES and 1 mM EDTA). For SPC, a 2 mL glass Dounce homogenizer with teflon pestle (Fisher Scientific 22-290067) was used; for brain, a 7 mL glass Dounce homogenizer (Fisher Scientific K885303-0007) was used with a teflon pestle (MilliporeSigma P7859). The homogenate was diluted 1:1 in Washing Buffer [210 mM mannitol, 70 mM sucrose, 5 mM HEPES and 1 mM EDTA, 0.5% fatty acid-free (FAF)-BSA (MilliporeSigma A7511), pH 7.2], and centrifuged at 900 × *g* for 10 min at 4 °C. The supernatant was centrifuged at 9000 × *g* for 10 min at 4 °C. The resulting pellets were resuspended in homogenization buffer and centrifuged again at 9000 × *g* for 10 min at 4 °C, and protein concentration was measured using the Quick Start Bradford Protein Assay Kit 1 (Bio-Rad 5000201). Mitochondrial respiration was measured in Mitochondrial Assay Solution (MAS: 70 mM sucrose, 220 mM mannitol, 5 mM KH_2PO_4, 5 mM $MgCl_2$, 2 mM HEPES, 1 mM EGTA, 0.2% FAF-BSA, pH 7.4 adjusted with 1 M KOH). Stock solutions containing 10X substrate stocks were prepared as follows: for complex I (CI)-driven respiration, 50 mM pyruvate (MilliporeSigma P2256) + 50 mM malate (MilliporeSigma M8304); for Complex II (CII)-driven respiration, 50 mM succinate (MilliporeSigma S2378) + 20 μM rotenone (MilliporeSigma 557368) (final concentration of each substrate was 5 mM for pyruvate/malate/succinate and 2 μM for rotenone). For CI-mediated respiration, 8 μg protein was resuspended in MAS + CI substrates; for CII-mediated respiration, 6 μg protein was resuspended in MAS + CII substrates, all in a final volume of 50 μL. The plate was centrifuged at 2000 × *g* for 5 min at 4 °C, and 450 μL additional buffer was added to each well. In blank wells, 500 μL MAS was added. Oxygen consumption was measured at States 2, 3, 4, and 3-uncoupled (3U) after sequential addition of 3 mM ADP (MilliporeSigma A5285), 4 μM oligomycin A (MilliporeSigma 75351), 6 μM carbonyl-cyanide p-triflouromethoxyphenylhydrazone (FCCP) (MilliporeSigma C2920) and 4.5 μM antimycin A (MilliporeSigma A8674), respectively.

Whole cells: 50,000 cells were seeded in each well of a 24-well Seahorse assay plate and differentiated to motor neurons for days in vitro (DIV) 2, DIV5, and DIV14. OCR was measured under basal conditions (Seahorse media with 2 mM pyruvate and 25 mM glucose) and after the sequential addition of 1 μM oligomycin A, 0.75 μM FCCP, and 1 μM rotenone + 1 μM antimycin A. Protein concentration was measured in each well after the experiment and all OCR values were normalized accordingly.

Permeabilized cells: 50,000 cells were seeded in each well of a 24-well Seahorse assay plate. The culture medium was replaced with MAS buffer containing 10 nM XF plasma membrane permeabilizer (PMP) reagent (Agilent Technologies 102504–100) with 5 mM malate + 5 mM pyruvate (for complex I assays) or 5 mM succinate + 2 μM rotenone (for complex II assays). OCR was measured with no added substrates (state 2), and then after the sequential addition of 3 mM ADP (state 3), 4 μM oligomycin A (state 4), and 6 μM FCCP (state 3-uncoupled).

Co-staining for COX and SDH activities

Mice were sacrificed by decapitation at P60. The SPC was extracted and immediately snap-frozen in isopentane at − 40 °C for 35 sec. Following storage at − 80 °C, the SPCs were sectioned at 20 μm thickness using a cryostat (Leica Biosystems CM3050 S). The sections were stored at − 80 °C until ready for sequential staining, at which point they were equilibrated at room temperature (RT) for 30 min before initiation of the staining protocol. The staining solution consisted of 2.7 mM 3,3-diaminobenzidine (DAB, MilliporeSigma D5637), 0.09 mM cytochrome *c* from the equine heart (MilliporeSigma C7752), and 3 μg/mL catalase (MilliporeSigma C1345) in 5 mM phosphate buffer, pH 7.4, filtered through Whatman paper. 100–200 μL of staining solution was applied onto tissue sections for 40 min at 37 °C in the dark, followed by 4 washes for 10 min each with ddH_2O. Following completion of the COX staining protocol, the samples were subjected to SDH staining. The solution consisted of 5 mM EDTA, 1 mM KCN, 0.2 mM phenazine methosulfate (MilliporeSigma P9625), 50 mM succinic acid (MilliporeSigma 398055), and 1.5 mM nitrotetrazolium blue chloride (MilliporeSigma N6876) in 5 mM phosphate buffer, pH 7.6, filtered through Whatman paper. The stain was applied to the tissues for 40 min at 37 °C in the dark, followed by 4 washes of 10 min each with ddH_2O. The slides were covered with warmed glycerin jelly as a mounting medium. Images were collected the next day using a Nikon Eclipse 80i brightfield microscope[35].

Enzymatic activity assays

Complex II activity. This assay was conducted as previously described[51]. Complex II-dependent activity was measured in a plate reader (SpectraMax M2, Molecular Devices) recorded as the reduction of 2,6-dichloroindophenol (DCIP, MilliporeSigma D1878) as the chromophore (100 μM, 600 nm, $\varepsilon = 21\ mM^{-1}\ cm^{-1}$, blue to colorless) in HEPES buffer containing 60 μM DCIP, 40 μM decylubiquinone Q1 (MilliporeSigma D7911), 0.5 μg/mL alamethicin (Cayman Chemical 11425), 2.5 μM rotenone and 20 mM succinate. When required, ubiquinol oxidation by the respiratory chain was inhibited by 1 mM KCN, and

1.5 nM atpenin A5 (Cayman Chemical 11898) was used to inhibit complex II. The rate of the corresponding blank was subtracted from each corresponding sample.

HK/PDHC/LDH activities. Enzymatic activities were measured following manufacturer instructions using commercial colorimetric quantification kits for hexokinase (HK; MilliporeSigma MAK091), pyruvate dehydrogenase (PDHC, BioVision K679-100), and lactate dehydrogenase (LDH, BioVision K726-500). For HK activity, we used 1×10^6 hMNs, 100 μg mouse SPC tissue, or 200 μg mouse brain tissue for each sample. For PDHC activity, we used 15–20 μg of total homogenates from hMNs, 40 μg mouse SPC tissue, or 100 μg mouse brain tissue for each sample. For LDH activity, we used 20 μg of total homogenates from hMNs for each sample. For all assays, absorbance at 450 nm was measured using a Tecan Infinite 200 Pro plate reader at multiple time points.

CPT1 activity. The carnitine palmitoyl transferase-1 (CPT1) assay was performed as described previously[89] with modifications. Briefly, 200 μg of crude mitochondria protein (isolated using the same procedure as for the bioenergetics analyses) was added to the assay medium containing 20 mM HEPES (pH 7.3), 75 mM KCl, 2 mM KCN, 1% FAF-BSA, 70 μM palmitoyl-CoA (MilliporeSigma P9716), and 0.25 mM L-[^{14}C] carnitine (PerkinElmer NEC797010UC), with or without 100 μM malonyl-CoA (MilliporeSigma M4263). Samples were incubated at 37 °C for 10 min. The reaction was stopped by the addition of 500 μL of 1 M ice-cold perchloric acid. Mitochondria were centrifuged at 12,000 x *g* for 2 min, the pellet was washed with 500 μL of 2 mM perchloric acid, and centrifugation was repeated. The resulting pellet was resuspended in 800 μL ddH_2O and extracted with 600 μL butanol. 300 μL of the butanol phase was transferred to scintillation vials containing 3 mL ScintiVerse BD Cocktail (Fisher Scientific SX18-4). The vials were vortexed and ^{14}C radioactivity was measured in a scintillation counter (Tri-Carb 2819TR, Perkin Elmer).

Sphingomyelinase treatment. Cells were incubated with 1 unit/mL of exogenous sphingomyelinase (SMase) from *Bacillus cereus* (MilliporeSigma S9396) for 1 h at 37 °C in neuronal differentiation media (described above). After incubation, the media was replaced and downstream analyses were performed.

Phospholipid synthesis and transfer

For assays in cultured cells, the cells were incubated for 2 h in MEM (ThermoFisher Scientific 11095098). The medium was replaced with MEM containing 2.5 μCi/mL ^{3}H-serine (PerkinElmer NET248005MC), and cell pellets were collected after 2, 4, or 6 h. The cells were washed and collected in 1X PBS, pelleted at 2500 × *g* for 5 min at 4 °C, and resuspended in 500 μL ddH_2O, removing a small aliquot for protein quantification. For assays in crude mitochondria fractions, the mitochondria were isolated using the same procedure as for the bioenergetics analyses. 50–100 μg of crude mitochondria were incubated in mitochondrial buffer containing 225 mM mannitol, 25 mM HEPES, and 1 mM EGTA (pH 7.4) supplemented with 5 μCi/mL ^{3}H-serine at 37 °C for 10 min. For both cultured-cell and crude mitochondria assays, lipid extraction was done using the Bligh and Dyer method[90]. Briefly, 18 volumes of 1:2 chloroform:methanol were added to the samples and vortexed. After centrifugation at 8000 × *g* for 5 min, the supernatant was transferred to a clean tube, and 6 volumes of chilled chloroform followed by 5 volumes of chilled ddH_2O were added to the tube, vortexed, and centrifuged again at 9000 × *g* for 2 min. The organic phase was transferred to a clean tube, concentrated, and re-extracted in 10 volumes of chilled chloroform, vortexed and centrifuged at 8000 × *g* for 2 min. Finally, the organic phase was transferred to a clean tube and dried under nitrogen gas. Dried lipids were resuspended in 100 μL 1:1 chloroform:methanol and spotted onto a silica thin layer chromatography (TLC) plate (Supleco Z740235). Phospholipids were separated using two solvents, composed of petroleum ether:diethyl ether:acetic acid 84:15:1 (v/v/v) and chloroform:methanol:acetic acid:water 60:50:1:4 (v/v/v/v). The TLC plate was developed by exposure to iodine vapor. The spots corresponding to the relevant phospholipids (identified using co-migrating standards) were cut from the TLC plate and transferred to a scintillation vial containing 3 mL ScintiVerse BD Cocktail. The vials were vortexed and ^{3}H radioactivity was measured in a scintillation counter.

Kinetics of complex-I D-form activation

Mice were sacrificed, and tissues (brains and SPC) were removed immediately, snap-frozen in liquid nitrogen, and stored at − 80 °C. 60-80 mg of tissue was homogenized using a glass Dounce homogenizer in 2 mL SET buffer (250 mM sucrose, 0.2 mM EDTA, 50 mM Tris-HCl, pH 8.8). The homogenization media was supplemented with 50 μg/mL alamethicin (Cayman Chemical 11425) and 1 mM fericyanide (for the preservation of physiological CI-A/CI-D ratios during isolation, MilliporeSigma 702587). Samples were centrifuged at 1500 × *g* for 5 min at 40 °C. The remaining supernatant was centrifuged at 20,000 × *g* for 20 min at 4 °C, and the resulting pellet was washed twice with SET buffer (pH 8.0) and subsequently resuspended in 100 mL SET buffer (pH 7.5), aliquotted and stored at − 80 °C. At the time of the assay, mitochondrial samples were diluted to 2–5 mg/mL and resuspended in SET buffer (pH 8.5) supplemented with 5 mM $MgCl_2$ and 15–30 μg alamethicin. The preparation was split into two samples: one incubated at 35 °C for 30–60 min under constant shaking to convert the whole pool of complex I to the D form, and a second one kept at 4 °C. The activity was measured in SET buffer (pH 8.5) supplemented with 5 mM $MgCl_2$, 15–30 μg alamethicin (Cayman Chemical 11425), and 5 μg cytochrome c (MilliporeSigma C-7752) containing 15–25 μg of mitochondrial protein/mL. The enzymatic activity of complex I in the D- or A-form was triggered by the addition of 140 μM NADH (MilliporeSigma 10128023001) to the cuvette at 25 °C and measured spectrophotometrically (Cary 4000, Agilent Technologies) as a decrease in absorption at 340 nm (ε_{340} nm = 6.22 mM^{-1} cm^{-1})[19,82]. The first-rate order constant of the D-form to A-form transition was calculated in R version 3.4 (RStudio, Posit PBC) using semilogarithmic plots as described previously[19].

Measurement of mitochondrial H_2O_2 release in intact mitochondria

Mitochondrial respiration and H_2O_2 release were measured using a high-resolution respirometer (Oroboros Oxygraph-2k®) equipped with a two-channel fluorescence optical setup to use with the Amplex UltraRed and horseradish peroxidase assays[51]. In brief, mitochondria (0.1 mg) were incubated in 2 mL assay medium composed of 125 mM KCl, 0.2 mM EGTA, 20 mM HEPES-Tris, 4 mM KH_2PO_4 (pH 7.4), 2 mM $MgCl_2$, 1 mg/mL FAF-BSA, 10 mM Amplex UltraRed (ThermoFisher Scientific A36006), 10 U/mL SOD (MilliporeSigma S9697) and 4 U/mL horseradish peroxidase (ThermoFisher Scientific 012001) at 37 °C. To initiate respiration, 2 mM malate + 5 mM pyruvate or 5 mM succinate + 1 mM glutamate were used. The H_2O_2 assays were calibrated by adding 100-200 pmol aliquots of a fresh standard solution of H_2O_2 (ε_{240} nm = 46.3 M^{-1} cm^{-1})[51]. ROS release was normalized by oxygen consumption in the sample at the same time of ROS release, and the data were expressed as the average of at least 3 biological replicates each consisting of 3-4 technical replicates.

Quantification of NAD$^+$/NADH ratios

The NAD$^+$/NADH ratio was measured using a commercial quantification kit (MilliporeSigma MAK037) following manufacturer instructions. Briefly, to measure total NAD (NAD$^+$ and NADH), 150 μg of total homogenate from cells or 20 μg of total homogenate from tissues was resuspended in 400 μL extraction buffer. After two cycles of freeze/thawing and vortexing, the cell extract was filtered using a 10-kDa cut-off spin filter, and the filtrate was split into two 200-μL aliquots and kept on ice. To measure only NADH, 200 μL was incubated at 60 °C for 30 min (to decompose NAD$^+$), chilled, and centrifuged at 9000 × *g* for 15 min. When tissues were assayed, 3 NTg and 3 SOD1^{G93A} mice were sacrificed and their brains and SPCs were immediately removed and washed. 20 mg of brain or SPC tissues was homogenized in 400 mL extraction buffer and filtered using a 10-kDa filter. The filtrate was processed as described above for cell homogenates. Absorbance at 450 nm was measured using a Tecan Infinite 200 Pro plate reader at multiple time points. The data were represented as the ratio of total NAD (NAD$^+$ + NADH) to NADH alone, and relative to controls.

Plasmid constructs and transfections

For BioID assays, we constructed the plasmids pDEL066 (expressing myc-BioID2-hSOD1^{WT}) and pDEL067 (expressing myc-BioID2-hSOD1^{G93A}) using standard techniques. pDEL066 and pDEL067 were constructed by PCR amplification of pF141 pAcGFP1 SOD1WT (Addgene plasmid 26402; RRID: Addgene_26402) and pF145 pAcGFP1 SOD1G93A (Addgene plasmid 26406; RRID: Addgene_26406), respectively (gifts from Elizabeth Fisher; forward primer: EcoRI F_hSOD1 WT 5′-aaaGAATTCATGGCGACGAAGGCCGTG-3′; reverse primer: BamHI R_hSOD1 WT 5′-aaaGGATCCTTATTGGGCGATCCCAATTACAC-3′). PCR products were digested with EcoRI/BamHI restriction enzymes and ligated into the same restriction sites (underlined) of a myc-BioID2-MCS plasmid (Addgene plasmid 74223; RRID: Addgene_74223; a gift from Kyle Roux). Myc-BioID2-MCS empty vector was used as a control. For PhotoClick cholesterol assays, we used pF151 pcDNA3.1(+)SOD1WT (Addgene plasmid 26397; RRID: Addgene_26397) and pF155 pcDNA3.1(+)SOD1G93A (Addgene plasmid 26401; RRID: Addgene_26401), which were gifts from Elizabeth Fisher. A pcDNA3.1(+) empty vector plasmid was used as a control. Cells were transfected with these plasmids using Lipofectamine™ 2000 Transfection Reagent (ThermoFisher Scientific 11668500) in serum-free DMEM for 6 h according to manufacturer instructions (1 μg DNA/μL Lipofectamine™ 2000). All plasmids were verified by restriction digest analysis, Sanger sequencing and western blot for expression efficiency (Supplementary Fig. 7).

BioID assays

To examine the potential protein binding partners of ALS-related proteins at MAM, we used an unbiased proteomics assay called BioID2[62]. This method is based on proximity-dependent biotin labeling of protein binding partners. We subcloned hSOD1^{WT} and hSOD1^{G93A} fused to the C-terminus of a myc-BioID2 fusion protein (subcloning strategy described above). These plasmids were transfected into NSC-34 cells and, after 24 h, the cells were treated with 50 μM biotin for 3 h. Biotinylated proteins from total homogenates and MAM fractions (collected using the Subcellular Fractionation protocol described below) were purified by immunoprecipitation using streptavidin beads (Cell Signaling Technology 3419S), and the purified proteins were analyzed by proteomics[91] as described. Raw data were processed using Scaffold 3 Proteome Software, and the processed data were analyzed using the parametric Student's two-tailed *t*-test at an $\alpha = 0.05$ significance level, and significant fold changes between the indicated groups ($p<0.05$) were indicated with asterisks in heat maps and column graphs.

PhotoClick cholesterol assays

To validate the effect of mutations in *SOD1* on the architecture of MAM, we performed a PhotoClick cholesterol assay[92]. Briefly, 24 h after transfection, NSC-34 cells were incubated in serum-free medium for 2 h to remove all exogenous lipids. After that, 5 μM PhotoClick cholesterol (Hex-5′-ynyl 3β-hydroxy-6-diazirinyl-5α-cholan-24-oate, Avanti Research 700147P), previously complexed with an aqueous saturated solution of 38 mM methyl-β-cyclodextrin (MβCD, MilliporeSigma C4555), was added to the cells and incubated for 4 h. Upon washes with 1X PBS, PhotoClick cholesterol was crosslinked under 365 nm-UV (0.75 J/cm2, UVC 500 Ultraviolet Crosslinker, Amersham Biosciences), washed again, collected, and used for subcellular fractionation as previously described. 500 μg (adjusted to a final volume of 150 μL with PBS supplemented with protease inhibitors) of total homogenate or MAM fractions were briefly sonicated and subjected to click chemistry by addition of 500 μM biotin-azide, 100 μM Tris[(1-benzyl-1H-1,2,3-triazol-4-yl)methyl]amine (TBTA), 1 mM $CuSO_4$, and 1 mM Tris(2-carboxyethyl)phosphine (TCEP) and incubation for 15 min at room temperature in the dark. The samples were then diluted in 50 mM Tris pH 7.4 with protease inhibitors (removing an aliquot as input) and incubated overnight under rotation at 4 °C with streptavidin beads. Upon several washes with Tris 50 mM pH 7.4, beads were collected by centrifugation at 400 × *g* for 1 min. Each fraction was analyzed by proteomics[91] as described. Raw data were analyzed using Scaffold 3 Proteome Software, and the processed data were analyzed using the parametric Student's two-tailed *t*-test at an $\alpha = 0.05$ significance level, and significant fold changes between the indicated groups ($p<0.05$) were indicated with asterisks in heat maps.

Lipidomics analyses

Lipids were extracted from equal amounts of material (50-500 μg protein/sample). Lipid extracts were prepared via chloroform–methanol extraction, spiked with appropriate internal standards, and analyzed using a 6490 Triple Quadrupole LC/MS system (Agilent Technologies) as described previously[93]. Lipids were separated by normal-phase HPLC using an Agilent Zorbax Rx-Sil column (inner diameter 2.1 × 100 mm) under the following conditions: mobile phase A (chloroform:methanol:1 M ammonium hydroxide, 89.9:10:0.1, v/v/v) and mobile phase B (chloroform:methanol:water:-ammonium hydroxide, 55:39.9:5:0.1, v/v/v/v); 95% A for 2 min, linear gradient to 30% A over 18 min and held for 3 min, and linear gradient to 95% A over 2 min and held for 6 min. Quantification of lipid species was accomplished using multiple reaction monitoring (MRM) transitions that were developed in earlier studies[93] in conjunction with referencing of appropriate internal standards: ceramide d18:1/17:0 and sphingomyelin d18:1/12:0 (Avanti Polar Lipids). Values were represented as mole fractions with respect to total lipid (% molarity). For this, the lipid mass (in moles) of any specific lipid was normalized by the total mass (in moles) of all the lipids measured[93]. In addition, all of our results were further normalized by protein content. Intensity signals of each lipid species acquired from the lipidomics analysis were converted to concentration values based on the concentration of spiked internal standards of similar ionization efficiencies. The data were first normalized using the NOMIS approach to reduce any systematic variabilities, such as batch effects, as described by Sysi-Aho et al.[94] and implemented in the "metabolomics" R package in RStudio 3.4. The normalized data were used to draw a principal component analysis (PCA) graph to confirm the removal of systematic variations as well as to detect any possible outliers that would be subject to biological interpretation. No clustering was observed, indicating removal of systematic variabilities by normalization. Samples outside the confidence level of 95% were removed from the data set for analysis. The data were analyzed using the parametric Student's two-tailed *t*-test at

an $\alpha = 0.05$ significance level, and significant fold changes ($p<0.05$) between the indicated groups were indicated with asterisks in heat maps and column graphs.

Quantitative reverse transcription polymerase chain reaction (qRT–PCR)

Total RNA was extracted from fresh tissues or cells using TRIzol™ Reagent (ThermoFisher Scientific 15596018) according to manufacturer instructions and was quantified by NanoDrop 2000 (ThermoFisher Scientific). 1–5 μg of RNA was digested with DNase (Promega M6101) and reverse-transcribed to cDNA using the High-Capacity cDNA Reverse Transcription Kit (ThermoFisher Scientific 4368813). Quantitative RT-PCR was performed in triplicate in a StepOnePlus™ Real-Time PCR System (ThermoFisher Scientific 4376600). The expression of each gene under study was analyzed using specific predesigned TaqMan™ probes from ThermoFisher Scientific (FAM/MGB): *PPARGC1A* (Hs00173304_m), *Ppargc1a* (Mm01208835_m1), *LDHA* (Hs01378790_g1), *CPT1A* (Hs00912671_m), *Hk1* (Mm00439344_m1) and *Hk2* (Mm00443385_m1). As the housekeeper genes, we used primer-limited VIC/MGB probes for *GAPDH* (Hs99999905_m1), *Gapdh* (Mm99999915_g1), and *18S rRNA* (4319413E). Measurement of the mitochondrial DNA (mtDNA):nuclear DNA (nDNA) ratio was performed using the following combinations of custom primers and probes. For human mtDNA:nDNA, we used: mtDNA_F 5'-CCACGGGAAACAGCAGTGATT-3' and mtDNA_R 5'-CTATTGACTTGGGTTAATCGTGTGA-3' (final concentration: 900 nM); and a custom TaqMan™ probe: FAM-TGCCAGCCACCGCG-MGB (final concentration: 200 nM). For nDNA, we used the TaqMan™ RNase P Control Reagents Kit (VIC, ThermoFisher Scientific 4316844). For mouse mtDNA:nDNA, we used: mtDNA_F 5'-TGCTAGCCGCAGGCATTACT-3' and mtDNA_R: 5'-CGGGATCAAAGAAAGTTGTGTTT-3' (final concentration: 900 nM); and a custom TaqMan™ probe: FAM-TACTACTAACAGACCGCAACC-MGB (final concentration: 200 nM). For nDNA, we measured *Gapdh* (VIC, Mm99999915_g1).

Subcellular fractionation and western blotting

Purification of MAM and mitochondria was performed and analyzed as described[58]. Western blot analysis was performed as described[95]. Blocking was done with 5% non-fat dry milk in 1X PBS, and primary/secondary antibodies were diluted in 1% non-fat dry milk in 1X PBS. We used primary antibodies recognizing beta-actin (clone BA3R, ThermoFisher Scientific MA5-15739, 1:2000 dilution), Erlin2 (Cell Signaling Technology 2959, 1:1000), MFN2 (Abcam ab50838, 1:1000), Myc-Tag (clone 71D10, Cell Signaling Technology 2278, 1:2000), SOD1 (Calbiochem 574597, 1:2000), TOM20 (Santa Cruz Biotechnology sc-11415, 1:1000) and beta-tubulin (clone AA2, MilliporeSigma T8328, 1:1000). To detect mitochondrial respiratory complexes, we heated samples at 50 °C and used Total OXPHOS Rodent WB Antibody Cocktail (Abcam ab110413, 1:250). As secondary antibodies, we used horseradish peroxidase-linked anti-rabbit IgG (Cytiva NA934-1ML, 1:10000), anti-mouse IgG (Cytiva NA931-1ML, 1:10000) or anti-sheep IgG (ThermoFisher Scientific 31480, 1:10000). Detection was done with SuperSignal™ West Dura Extended Duration Substrate (ThermoFisher Scientific 34075). Additional details about these antibodies, including validation data, can be found in Supplementary Information.

Filipin staining

Human MNs were grown on coverslips and fixed with 4% PFA for 30 min. After 3 washes with 1X PBS, PFA was quenched by incubating the cells with 1.5 mg glycine/mL PBS for 10 min. The cells were stained with filipin complex (MilliporeSigma F9765) at a concentration of 0.5 mg/mL in PBS with 10% FBS for 2 h at room temperature. After extensive washes, coverslips were mounted with Fluoromount-G™ (ThermoFisher Scientific 00-4958-02) and imaged using a Zeiss Axiovert Fluorescence Microscope with a UV filter cube (340–380 nm excitation, 40 nm dichroic, 430 nm long pass filter) to detect filipin and a FITC filter cube (488 nm excitation and 509 nm emission) to detect GFP expressed under the HB9 promoter.

Statistical analysis

All averages reflect 3 or more independent experiments. Each experiment consisted of different sets of samples that were measured at the same time within the same age group. Since we had a small sample size of 4-5 biological replicates, determining the distribution of the mean was important for choosing an appropriate statistical method. Therefore, a Shapiro-Wilk test was performed to assess normality. Based on the outcome, the data was analyzed using the parametric Student's two-tailed *t*-test for normal data or the non-parametric Mann-Whitney *U* test for non-normal data, at an $\alpha=0.05$ significance level. Unless otherwise indicated, the significance was expressed as n.s. $p>0.05$; * $p<0.05$; ** $p<0.01$; *** $p<0.001$; **** $p<0.0001$. All error bars in the figures represent SD among biological replicates or SE when showing technical replicates. All statistical analyses were performed using Microsoft Excel 2021 and GraphPad Prism 10.0e, and each biological replicate was normalized by control values of the same replicate within the same time intervals.

Reporting summary

Further information on research design is available in the Nature Portfolio Reporting Summary linked to this article.

Data availability

The proteomics datasets have been deposited into the PRIDE database with accession numbers PXD053415 and PXD053253. The lipidomics data is available in Zenodo [https://doi.org/10.5281/zenodo.12543984]. These data are also provided in the Supplementary Information/Source Data files. All reagents used in this work are commercially available, with manufacturer catalog numbers included in the Methods section. Source data are provided with this paper.

References

1. Rowland, L. P. & Shneider, N. A. Amyotrophic lateral sclerosis. *N. Engl. J. Med.* **344**, 1688–1700 (2001).
2. Goutman, S. A. et al. Emerging insights into the complex genetics and pathophysiology of amyotrophic lateral sclerosis. *Lancet Neurol.* **21**, 465–479 (2022).
3. Ghiasi, P., Hosseinkhani, S., Noori, A., Nafissi, S. & Khajeh, K. Mitochondrial complex I deficiency and ATP/ADP ratio in lymphocytes of amyotrophic lateral sclerosis patients. *Neurol. Res.* **34**, 297–303 (2012).
4. Smith, E. F., Shaw, P. J. & De Vos, K. J. The role of mitochondria in amyotrophic lateral sclerosis. *Neurosci. Lett.* **710**, 132933 (2019).
5. Goodpaster, B. H. & Sparks, L. M. Metabolic flexibility in health and disease. *Cell Metab.* **25**, 1027–1036 (2017).
6. Tefera, T. W., Steyn, F. J., Ngo, S. T. & Borges, K. CNS glucose metabolism in Amyotrophic Lateral Sclerosis: a therapeutic target? *Cell Biosci.* **11**, 14 (2021).
7. Dodge, J. C. et al. Metabolic signatures of amyotrophic lateral sclerosis reveal insights into disease pathogenesis. *Proc. Natl. Acad. Sci. USA* **110**, 10812–10817 (2013).
8. Pradat, P. F. et al. Impaired glucose tolerance in patients with amyotrophic lateral sclerosis. *Amyotroph. Lateral Scler.* **11**, 166–171 (2010).
9. Hirst, J. Mitochondrial complex I. *Annu. Rev. Biochem.* **82**, 551–575 (2013).

10. Dröse, S., Brandt, U. & Wittig, I. Mitochondrial respiratory chain complexes as sources and targets of thiol-based redox-regulation. *Biochim. Biophys. Acta.* **1844**, 1344–1354 (2014).
11. Speijer, D. Oxygen radicals shaping evolution: why fatty acid catabolism leads to peroxisomes while neurons do without it: $FADH_2$/NADH flux ratios determining mitochondrial radical formation were crucial for the eukaryotic invention of peroxisomes and catabolic tissue differentiation. *Bioessays* **33**, 88–94 (2011).
12. Speijer, D. How the mitochondrion was shaped by radical differences in substrates: what carnitine shuttles and uncoupling tell us about mitochondrial evolution in response to ROS. *Bioessays* **36**, 634–643 (2014).
13. Belanger, M., Allaman, I. & Magistretti, P. J. Brain energy metabolism: focus on astrocyte-neuron metabolic cooperation. *Cell Metab.* **14**, 724–738 (2011).
14. Mergenthaler, P., Lindauer, U., Dienel, G. A. & Meisel, A. Sugar for the brain: the role of glucose in physiological and pathological brain function. *Trends Neurosci.* **36**, 587–597 (2013).
15. Divakaruni, A. S. et al. Inhibition of the mitochondrial pyruvate carrier protects from excitotoxic neuronal death. *J. Cell Biol.* **216**, 1091–1105 (2017).
16. Chouchani, E. T. et al. Ischaemic accumulation of succinate controls reperfusion injury through mitochondrial ROS. *Nature* **515**, 431–435 (2014).
17. Robb, E. L. et al. Control of mitochondrial superoxide production by reverse electron transport at complex I. *J. Biol. Chem.* **293**, 9869–9879 (2018).
18. Pryde, K. R., Taanman, J. W. & Schapira, A. H. A LON-ClpP Proteolytic Axis Degrades Complex I to Extinguish ROS Production in Depolarized Mitochondria. *Cell Rep.* **17**, 2522–2531 (2016).
19. Dröse, S., Stepanova, A. & Galkin, A. Ischemic A/D transition of mitochondrial complex I and its role in ROS generation. *Biochim. Biophys. Acta.* **1857**, 946–957 (2016).
20. Bartlett, K. & Eaton, S. Mitochondrial beta-oxidation. *Eur. J. Biochem.* **271**, 462–469 (2004).
21. Berthiaume J. M., Kurdys J. G., Muntean D. M., Rosca M. G. Mitochondrial N. A. D. *Antioxid. Redox Signal.* **30**, 375–398 (2019).
22. Tubbs, E. et al. Mitochondria-associated endoplasmic reticulum membrane (MAM) integrity is required for insulin signaling and is implicated in hepatic insulin resistance. *Diabetes* **63**, 3279–3294 (2014).
23. Rieusset, J. The role of endoplasmic reticulum-mitochondria contact sites in the control of glucose homeostasis: an update. *Cell Death Dis.* **9**, 388 (2018).
24. Vance, J. E. MAM (mitochondria-associated membranes) in mammalian cells: Lipids and beyond. *Biochim. Biophys. Acta.* **1841**, 595–609 (2014).
25. Paillusson, S. et al. There's Something Wrong with my MAM; the ER-Mitochondria Axis and Neurodegenerative Diseases. *Trends Neurosci.* **39**, 146–157 (2016).
26. Guardia-Laguarta, C. et al. alpha-Synuclein is localized to mitochondria-associated ER membranes. *J Neurosci.* **34**, 249–259 (2014).
27. Pera, M. et al. MAM and C99, key players in the pathogenesis of Alzheimer's disease. *Int. Rev .Neurobiol.* **154**, 235–278 (2020).
28. Watanabe, S. et al. Mitochondria-associated membrane collapse is a common pathomechanism in SIGMAR1- and SOD1-linked ALS. *EMBO Mol. Med.* **8**, 1421–1437 (2016).
29. Stoica, R. et al. ER-mitochondria associations are regulated by the VAPB-PTPIP51 interaction and are disrupted by ALS/FTD-associated TDP-43. *Nat. Commun.* **5**, 3996 (2014).
30. Bernal, A. F., Mota, N., Pamplona, R., Area-Gomez, E. & Portero-Otin, M. Hakuna MAM-Tata: Investigating the role of mitochondrial-associated membranes in ALS. *Biochim. Biophys. Acta Mol. Basis Dis.* **1869**, 166716 (2023).
31. Crugnola, V. et al. Mitochondrial respiratory chain dysfunction in muscle from patients with amyotrophic lateral sclerosis. *Arch Neurol.* **67**, 849–854 (2010).
32. Manfredi, G. & Xu, Z. Mitochondrial dysfunction and its role in motor neuron degeneration in ALS. *Mitochondrion.* **5**, 77–87 (2005).
33. Bartolome, F. et al. Pathogenic VCP mutations induce mitochondrial uncoupling and reduced ATP levels. *Neuron.* **78**, 57–64 (2013).
34. Bonilla, E. et al. New morphological approaches to the study of mitochondrial encephalomyopathies. *Brain Pathol.* **2**, 113–119 (1992).
35. Franco-Iborra, S. & Tanji, K. Histochemical and immunohistochemical staining methods to visualize mitochondrial proteins and activity. *Methods Cell Biol.* **155**, 247–270 (2020).
36. Scaricamazza, S. et al. Skeletal-Muscle Metabolic Reprogramming in ALS-SOD1. *iScience* **23**, 101087 (2020).
37. Hall, E. D., Oostveen, J. A. & Gurney, M. E. Relationship of microglial and astrocytic activation to disease onset and progression in a transgenic model of familial ALS. *Glia.* **23**, 249–256 (1998).
38. Schonfeld, P. & Reiser, G. Why does brain metabolism not favor burning of fatty acids to provide energy? Reflections on disadvantages of the use of free fatty acids as fuel for brain. *J. Cereb. Blood Flow Metab.* **33**, 1493–1499 (2013).
39. Martínez-Reyes, I. & Chandel, N. S. Mitochondrial TCA cycle metabolites control physiology and disease. *Nat. Commun.* **11**, 102 (2020).
40. Wiedemann, F. R., Manfredi, G., Mawrin, C., Beal, M. F. & Schon, E. A. Mitochondrial DNA and respiratory chain function in spinal cords of ALS patients. *J. Neurochem.* **80**, 616–625 (2002).
41. Area-Gomez, E., Guardia-Laguarta, C., Schon, E. A. & Przedborski, S. Mitochondria, OxPhos, and neurodegeneration: cells are not just running out of gas. *J. Clin. Invest.* **129**, 34–45 (2019).
42. Brand, M. D. & Nicholls, D. G. Assessing mitochondrial dysfunction in cells. *Biochem. J.* **435**, 297–312 (2011).
43. Scialo, F., Fernandez-Ayala, D. J. & Sanz, A. Role of mitochondrial reverse electron transport in ROS signaling: potential roles in health and disease. *Front. Physiol.* **8**, 428 (2017).
44. Szelechowski, M. et al. Metabolic reprogramming in Amyotrophic Lateral Sclerosis. *Sci. Rep.* **8**, 3953 (2018).
45. Palamiuc, L. et al. A metabolic switch toward lipid use in glycolytic muscle is an early pathologic event in a mouse model of amyotrophic lateral sclerosis. *EMBO Mol. Med.* **7**, 526–546 (2015).
46. Adeva-Andany, M. M., Carneiro-Freire, N., Seco-Filgueira, M., Fernández-Fernández, C. & Mouriño-Bayolo, D. Mitochondrial β-oxidation of saturated fatty acids in humans. *Mitochondrion* **46**, 73–90 (2019).
47. Koves, T. R. et al. Mitochondrial overload and incomplete fatty acid oxidation contribute to skeletal muscle insulin resistance. *Cell Metab.* **7**, 45–56 (2008).
48. Acin-Perez, R. & Enriquez, J. A. The function of the respiratory supercomplexes: the plasticity model. *Biochim. Biophys. Acta.* **1837**, 444–450 (2014).
49. Guaras, A. et al. The CoQH2/CoQ ratio serves as a sensor of respiratory chain efficiency. *Cell Rep.* **15**, 197–209 (2016).
50. Nicholls D. G. *Bioenergetics*. 4t 4th Edition - May 20, 2013 Paperback ISBN: 9780123884251 9 7 8 - 0 - 1 2 - 3 8 8 4 2 5 - 1 eBook ISBN: 9780123884312 (2013).
51. Stepanova, A. et al. Deactivation of mitochondrial complex I after hypoxia-ischemia in the immature brain. *J. Cereb. Blood Flow Metab.* **39**, 1790–1802 (2019).
52. Panov, A. V. et al. Metabolic and functional differences between brain and spinal cord mitochondria underlie different predisposition to pathology. *Am. J. Physiol. Regul. Integr. Comp. Physiol.* **300**, R844–R854 (2011).

53. Betz, C. et al. Feature Article: mTOR complex 2-Akt signaling at mitochondria-associated endoplasmic reticulum membranes (MAM) regulates mitochondrial physiology. *Proc. Natl. Acad. Sci USA* **110**, 12526–12534 (2013).
54. Ciscato, F., Ferrone, L., Masgras, I., Laquatra, C. & Rasola, A. Hexokinase 2 in cancer: A prima donna playing multiple characters. *Int. J. Mol. Sci.* **22**, 4716 (2021).
55. Montesinos, J., Area-Gomez, E. & Schlame, M. Analysis of phospholipid synthesis in mitochondria. *Methods Cell Biol.* **155**, 321–335 (2020).
56. de Brito, O. M. & Scorrano, L. Mitofusin 2 tethers endoplasmic reticulum to mitochondria. *Nature* **456**, 605–610 (2008).
57. Lingwood, D. & Simons, K. Lipid rafts as a membrane-organizing principle. *Science* **327**, 46–50 (2010).
58. Area-Gomez, E. et al. Upregulated function of mitochondria-associated ER membranes in Alzheimer disease. *EMBO J.* **31**, 4106–4123 (2012).
59. Pera, M. et al. Increased localization of APP-C99 in mitochondria-associated ER membranes causes mitochondrial dysfunction in Alzheimer disease. *EMBO J.* **36**, 3356–3371 (2017).
60. Montesinos J. et al. The Alzheimer's disease-associated C99 fragment of APP regulates cellular cholesterol trafficking. *EMBO J.* **39**, e103791 (2020).
61. Rossi, A. et al. Defective mitochondrial pyruvate flux affects cell bioenergetics in Alzheimer's disease-related models. *Cell Rep.* **30**, 2332–2348 (2020).
62. Kim, DI. et al. An improved smaller biotin ligase for BioID proximity labeling. *Mol Biol Cell.* **27**, 1188–96 (2016).
63. Slotte, J. P. & Bierman, E. L. Depletion of plasma-membrane sphingomyelin rapidly alters the distribution of cholesterol between plasma membranes and intracellular cholesterol pools in cultured fibroblasts. *Biochem. J.* **250**, 653–658 (1988).
64. Infante, R. E. & Radhakrishnan, A. Continuous transport of a small fraction of plasma membrane cholesterol to endoplasmic reticulum regulates total cellular cholesterol. *Elife.***6**, e25466 (2017).
65. Parakh, S. & Atkin, J. D. The mitochondrial-associated ER membrane (MAM) compartment and its dysregulation in Amyotrophic Lateral Sclerosis (ALS). *Semin. Cell Dev. Biol.* **112**, 105–113 (2021).
66. Wang, W. et al. The ALS disease-associated mutant TDP-43 impairs mitochondrial dynamics and function in motor neurons. *Hum. Mol. Genet.* **22**, 4706–4719 (2013).
67. Townsend, L. K., Brunetta, H. S. & Mori, M. A. S. Mitochondria-associated ER membranes in glucose homeostasis and insulin resistance. *Am. J. Physiol. Endocrinol. Metab.* **319**, E1053–E1060 (2020).
68. Tubbs, E. et al. Disruption of mitochondria-associated endoplasmic reticulum membrane (MAM) integrity contributes to muscle insulin resistance in mice and humans. *Diabetes.* **67**, 636–650 (2018).
69. Mariosa, D. et al. Body mass index and Amyotrophic Lateral Sclerosis: A study of US military veterans. *Am. J. Epidemiol.* **185**, 362–371 (2017).
70. Mariosa, D. et al. Blood biomarkers of carbohydrate, lipid, and apolipoprotein metabolisms and risk of amyotrophic lateral sclerosis: A more than 20-year follow-up of the Swedish AMORIS cohort. *Ann. Neurol.* **81**, 718–728 (2017).
71. Dorst, J. et al. Patients with elevated triglyceride and cholesterol serum levels have a prolonged survival in amyotrophic lateral sclerosis. *J. Neurol.* **258**, 613–617 (2011).
72. Moll, T., Shaw, P. J. & Cooper-Knock, J. Disrupted glycosylation of lipids and proteins is a cause of neurodegeneration. *Brain* **143**, 1332–1340 (2020).
73. Area-Gomez, E. et al. Lipidomics study of plasma from patients suggest that ALS and PLS are part of a continuum of motor neuron disorders. *Sci. Rep.* **11**, 13562 (2021).
74. Zhao, W. et al. Caprylic triglyceride as a novel therapeutic approach to effectively improve the performance and attenuate the symptoms due to the motor neuron loss in ALS disease. *PLoS ONE* **7**, e49191 (2012).
75. Nicholls, D. G., Rugolo, M., Scott, I. G. & Meldolesi, J. alpha-latrotoxin of black widow spider venom depolarizes the plasma membrane, induces massive calcium influx, and stimulates transmitter release in guinea pig brain synaptosomes. *Proc. Natl. Acad. Sci. USA* **79**, 7924–7928 (1982).
76. Luengo, A. et al. Increased demand for NAD. *Mol. Cell* **81**, 691–707.e6 (2021).
77. Pryde, K. R. & Hirst, J. Superoxide is produced by the reduced flavin in mitochondrial complex I: a single, unified mechanism that applies during both forward and reverse electron transfer. *J. Biol. Chem.* **286**, 18056–18065 (2011).
78. Dell'Orco, M. et al. Hydrogen peroxide-mediated induction of SOD1 gene transcription is independent from Nrf2 in a cellular model of neurodegeneration. *Biochim. Biophys. Acta* **1859**, 315–323 (2016).
79. Gagliardi, S. et al. SOD1 mRNA expression in sporadic amyotrophic lateral sclerosis. *Neurobiol. Dis.* **39**, 198–203 (2010).
80. Kaewpila, S., Venkataraman, S., Buettner, G. R. & Oberley, L. W. Manganese superoxide dismutase modulates hypoxia-inducible factor-1 alpha induction via superoxide. *Cancer Res.* **68**, 2781–2788 (2008).
81. Iwaya, S. et al. Suppressive effects of adaptive servo-ventilation on ventricular premature complexes with attenuation of sympathetic nervous activity in heart failure patients with sleep-disordered breathing. *Heart Vessels.* **29**, 470–477 (2014).
82. Galkin, A. & Moncada, S. S-nitrosation of mitochondrial complex I depends on its structural conformation. *J. Biol. Chem.* **282**, 37448–37453 (2007).
83. Estévez, A. G. et al. Induction of nitric oxide-dependent apoptosis in motor neurons by zinc-deficient superoxide dismutase. *Science* **286**, 2498–2500 (1999).
84. Singh, T. et al. Neuronal mitochondrial dysfunction in sporadic amyotrophic lateral sclerosis is developmentally regulated. *Sci. Rep.* **11**, 18916 (2021).
85. Obrador E., Salvador-Palmer R., López-Blanch R., Dellinger R. W., Estrela J. M. NAD. *Biomedicines* https://doi.org/10.3390/biomedicines9081000 (2021).
86. Thams, S. et al. A stem cell-based screening platform identifies compounds that desensitize motor neurons to endoplasmic reticulum stress. *Mol. Ther.* **27**, 87–101 (2019).
87. Di Giorgio, F. P., Boulting, G. L., Bobrowicz, S. & Eggan, K. C. Human embryonic stem cell-derived motor neurons are sensitive to the toxic effect of glial cells carrying an ALS-causing mutation. *Cell Stem Cell* **3**, 637–648 (2008).
88. Agrawal, R. R., Tamucci, K. A., Pera, M. & Larrea, D. Assessing mitochondrial respiratory bioenergetics in whole cells and isolated organelles by microplate respirometry. *Methods Cell Biol.* **155**, 157–180 (2020).
89. Bremer, J. The effect of fasting on the activity of liver carnitine palmitoyltransferase and its inhibition by malonyl-CoA. *Biochim. Biophys. Acta* **665**, 628–631 (1981).
90. BLIGH, E. G. & DYER, W. J. A rapid method of total lipid extraction and purification. *Can. J. Biochem. Physiol.* **37**, 911–917 (1959).
91. Chen J. et al. Juvenile CLN3 disease is a lysosomal cholesterol storage disorder: similarities with Niemann-Pick type C disease. *EBioMedicine.* **92**, 104628 (2023).
92. Hulce, J. J., Cognetta, A. B., Niphakis, M. J., Tully, S. E. & Cravatt, B. F. Proteome-wide mapping of cholesterol-interacting proteins in mammalian cells. *Nat. Methods.* **10**, 259–264 (2013).
93. Chan, R. B. et al. Comparative lipidomic analysis of mouse and human brain with Alzheimer disease. *J. Biol. Chem.* **287**, 2678–2688 (2012).

94. Sysi-Aho, M., Katajamaa, M., Yetukuri, L. & Oresic, M. Normalization method for metabolomics data using optimal selection of multiple internal standards. *BMC Bioinformatics* **8**, 93 (2007).
95. Larrea, D. et al. MFN2 mutations in Charcot-Marie-Tooth disease alter mitochondria-associated ER membrane function but do not impair bioenergetics. *Hum. Mol. Genet.* **28**, 1782–1800 (2019).

Acknowledgements

This work was supported by La Caixa Health Foundation and Fundación Luzón (HR23-00124 to EA-G), the Spanish Ministry of Science and Innovation (PID2021-126818NB-I00 to EA-G), Project ALS, the US National Institutes of Health (R01-AG056387 to EA-G; R21NS125466 and R01NS112381 to AG; T32-DK007647 to KAT and RRA; F31NS095571 to JWS), and the US Department of Defense (FA9550-11-C-0028 to RRA; W81XWH2210404 and W81XWH2110370 to ERL). We thank Eric A. Schon, Neil A. Shneider, and Serge Przedborski for their critical discussions. We thank James Caicedo and Norma Romero for laboratory assistance. We thank Barbara Corneo and the Columbia University Stem Cell Core facility for assistance in the handling and differentiation of iPSC lines. We thank Renu Nandakumar for assistance with the lipidomics analysis. We thank the Columbia University Proteomics and Structural Biology core facility for assistance with the proteomics analysis. Finally, we thank all members of the Motor Neuron Center at Columbia University Irving Medical Center for providing tissues and cells for analysis, and for helpful discussions and support.

Author contributions

Conceived the project: EA-G and DL. Designed experiments: DL and EA-G. Provided key reagents: ERL, JWS, HW, and CP. Generated data for most of the experiments: DL, KAT, KRV, KK, and MP. Critically assisted with complex I analysis: AS, BY-S and AG. Collected/analyzed lipidomics data: TDY and EA-G. Wrote the manuscript: DL and EA-G. Critically edited the manuscript: DL, RRA, KAT, JM, AG, and EA-G. Approved final version of the manuscript: all authors.

Competing interests

The authors declare no competing interests.

Additional information

Supplementary information The online version contains supplementary material available at https://doi.org/10.1038/s41467-024-51578-1.

Correspondence and requests for materials should be addressed to Delfina Larrea or Estela Area-Gomez.

Peer review information *Nature Communications* thanks the anonymous reviewers for their contribution to the peer review of this work. A peer review file is available.